SPECIAL DYNAMO/CINDY/AMIE/LASP COLLECTION

The Diurnal Variability of Precipitating Cloud Populations during DYNAMO

NAOKO SAKAEDA

School of Meteorology, University of Oklahoma, Norman, Oklahoma

SCOTT W. POWELL

Department of Atmospheric Science, Colorado State University, Fort Collins, Colorado

JULIANA DIAS

CIRES, University of Colorado Boulder, and NOAA/Earth System Research Laboratory, Boulder, Colorado

GEORGE N. KILADIS

Physical Sciences Division, NOAA/Earth System Research Laboratory, Boulder, Colorado

(Manuscript received 16 October 2017, in final form 28 January 2018)

ABSTRACT

This study uses high-resolution rainfall estimates from the S-Polka radar during the DYNAMO field campaign to examine variability of the diurnal cycle of rainfall associated with MJO convection over the Indian Ocean. Two types of diurnal rainfall peaks were found: 1) a late afternoon rainfall peak associated with the diurnal peak in sea surface temperatures (SSTs) and surface fluxes and 2) an early to late morning rainfall peak associated with increased low-tropospheric moisture. Both peaks appear during the MJO suppressed phase, which tends to have stronger SST warming in the afternoon, while the morning peak is dominant during the MJO enhanced phase. The morning peak occurs on average at 0000–0300 LST during the MJO suppressed phase, while it is delayed until 0400–0800 LST during the MJO enhanced phase. This delay partly results from an increased upscale growth of deep convection to broader stratiform rain regions during the MJO enhanced phase. During the MJO suppressed phase, rainfall is dominated by deep and isolated convective cells that are short-lived and peak in association with either the afternoon SST warming or nocturnal moisture increase. This study demonstrates that knowledge of the evolution of cloud and rain types is critical to explaining the diurnal cycle of rainfall and its variability. Some insights into the role of the complex interactions between radiation, moisture, and clouds in driving the diurnal cycle of rainfall are also discussed.

1. Introduction

Intraseasonal variability in the atmosphere bridges an important time scale between climate and weather. A key phenomenon that occurs on intraseasonal time scales in the tropics is the Madden–Julian oscillation (MJO; Madden and Julian 1971, 1972). The MJO is known to influence a wide range of spatial and temporal weather and climate phenomena (Lau and Waliser 2011), including the diurnal cycle of rain, which is the focus of this study. The diurnal cycle in precipitation is one of the fundamental modes of atmospheric variability, yet it is not completely understood what drives it or how it varies with large-scale atmospheric variability, especially over the open ocean (Yang and Slingo 2001). A number of studies have examined the relationship between the diurnal cycle of rainfall and the MJO (e.g., Sui et al. 1997; Chen and Houze 1997; Tian et al. 2006; Suzuki 2009; Fujita et al. 2011; Oh et al. 2012; Rauniyar and Walsh 2011; Sakaeda et al. 2017). However, many details of the relationship between the diurnal cycle of rainfall and the MJO remain to be answered. The physical processes underlying the relationship between the MJO and the diurnal evolution of cloud and rain types were unclear in Sakaeda et al. (2017) because the analysis was limited to satellite

Corresponding author: Naoko Sakaeda, nsakaeda@ou.edu

DOI: 10.1175/JAS-D-17-0312.1

estimates of cloud types and rain rates. Here we extend the results of Sakaeda et al. (2017) by using observations collected during the Dynamics of the MJO (DYNAMO; Yoneyama et al. 2013) field campaign to further examine the diurnal cycle by rain types and associated large-scale atmospheric variability.

It has been suggested that the interaction between the diurnal cycle and the MJO leads to a two-way feedback. A number of studies have shown that the amplitude of the diurnal cycle of rainfall and deep convection is enhanced within the enhanced convective envelope of the MJO, especially over the ocean (Sui et al. 1997; Chen and Houze 1997; Tian et al. 2006; Suzuki 2009; Fujita et al. 2011; Rauniyar and Walsh 2011; Sakaeda et al. 2017). Within the suppressed envelope of the MJO, isolated cumulus congestus clouds are more abundant than organized deep convection. Ruppert and Johnson (2015) and Ruppert (2016) suggested that the diurnal cycle of these cumulus congestus clouds during the suppressed phase of the MJO is important for moistening and preconditioning the troposphere for a new MJO convective initiation. Over the islands of the Maritime Continent, the amplitude of the diurnal cycle tends to peak a few days prior to the arrival of MJO convective centers (Sui and Lau 1992; Ichikawa and Yasunari 2006, 2008; Oh et al. 2012; Kanamori et al. 2013; Peatman et al. 2015; Sakaeda et al. 2017). The enhancement of the diurnal cycle prior to the arrival of the MJO led Peatman et al. (2014, 2015) to suggest that the diurnal cycle of rainfall may rectify onto intraseasonal time scales over the Maritime Continent, playing a role in MJO propagation over the region. Majda and Yang (2016) also suggested that the diurnal cycle feeds back onto the intraseasonal variability of temperature and momentum, partly generating the large-scale circulation consistent with the observed MJO. Therefore, the accurate representation of the diurnal cycle may be crucial for improving simulations of the MJO, since models frequently do not have realistic diurnal variability (Slingo et al. 2003; Peatman et al. 2015).

The diurnal cycle varies significantly depending on the cloud and rain types examined, such as high versus low clouds or heavy versus light rain rates (Albright et al. 1985; Janowiak et al. 1994; Chen and Houze 1997; Cairns 1995; Sakaeda et al. 2017). In past studies, clouds were generally categorized by infrared brightness temperature (Albright et al. 1985; Janowiak et al. 1994; Chen and Houze 1997) or cloud-top pressure estimated from brightness temperatures (Cairns 1995; Sakaeda et al. 2017). This method enables general classification of clouds by their height, but it cannot distinguish between deep convective cores and surrounding stratiform clouds within organized convective systems. Distinguishing between these cloud types (e.g., convective, stratiform) is important as they produce different vertical heating profiles, which yield different responses in the atmospheric circulation. Cloud populations generally evolve from isolated, shallow individual convective cells during the MJO suppressed phase to more organized, deep convective and stratiform clouds during the enhanced phase (Johnson et al. 1999; Kikuchi and Takayabu 2004; Barnes and Houze 2013; Zuluaga and Houze 2013; Powell and Houze 2013; Xu and Rutledge 2014; Powell and Houze 2015; Xu and Rutledge 2015). Sakaeda et al. (2017) showed that the increased stratiform rain following the deep convection tends to delay the peak timing of diurnal rainfall cycle within the convectively enhanced envelopes of the MJO compared to the suppressed envelopes. Therefore, further examination of how rain and cloud types vary diurnally and with the MJO is critical for a better understanding the diurnal cycle and its interactions with large-scale variability.

Over open tropical oceans, the diurnal cycle of rainfall tends to have peak total rainfall in the early morning hours, in contrast to the late afternoon peaks over land (Yang and Slingo 2001; Nesbitt and Zipser 2003; Kikuchi and Wang 2008). This early morning peak in rainfall over oceans has been proposed to be driven by several mechanisms such as 1) upper-tropospheric destabilization associated with nighttime radiative cooling at the top of clouds (Kraus 1963; Randall et al. 1991), 2) stronger radiative cooling of tropospheric temperature at night over clear than cloudy area that enhances low-level convergence into cloudy areas (Gray and Jacobson 1977), 3) greater tropospheric relative humidity and moisture at night (Sui et al. 1997; Frenkel et al. 2011), and 4) the life cycle of cloud systems that are triggered in the afternoon and develop into mesoscale convective systems (MCSs) that mature in the early morning hours (Chen and Houze 1997). While the climatological diurnal cycle of total rainfall is known to be largely contributed by the MCSs (Chen and Houze 1997; Nesbitt and Zipser 2003), the relative roles of the first three suggested mechanisms leading to their overnight development is unclear. By examining the variability in the diurnal cycle of rainfall and atmospheric profiles associated with the MJO, we aim to provide some insights into which of these proposed mechanisms explain the diurnal cycle of rainfall.

This study focuses on the relationship between the diurnal cycle of rainfall and the MJO over the tropical Indian Ocean, where the DYNAMO field campaign took place during October 2011–February 2012. The main objective of this field campaign was to collect intensive observations in order to analyze and understand MJO dynamics, especially its convective initiation processes. Three MJO events were observed during this field campaign. The DYNAMO data allow for a detailed examination of the diurnal cycle of rainfall and atmospheric conditions and their evolution during the passage of the three events. By taking advantage of the collected observations during DYNAMO, this study addresses three main questions:

1) How does the population of raining clouds evolve diurnally?
2) How does its diurnal cycle vary with the MJO?
3) What large-scale environmental factors are associated with changes in the diurnal cycle of rainfall?

2. Data and methodology

Radar and sounding-based data collected during DYNAMO are primarily used to examine the diurnal cycle of rainfall and atmospheric environmental conditions. Further details on the setup of the observational network during DYNAMO can be found in Yoneyama et al. (2013). Three-hourly, 0.25°-horizontal-resolution rainfall rates from the Tropical Rainfall Measuring Mission (TRMM) 3B42 version 7 (Huffman et al. 2007) are also used for comparison to the DYNAMO data in the appendix.

a. S-Polka radar-estimated rainfall rate and rain-type classification

The dual-polarimetric, dual-wavelength S-Polka radar from the National Center for Atmospheric Research (Keeler et al. 2000) utilizes wavelengths of 10 cm for the S-band and 0.8 cm for the Ka band, and is used here to identify rainfall and rain types. The radar was located at 0.63°S, 73.10°E, at Addu Atoll in the Maldives. The radar operated surveillance (SUR) scans at elevation angles between 0.5° and 11° and range–height indicator (RHI) scans that scanned at elevation angles up to 45° over azimuths ranging from 4° to 82° and 114° to 140° (Zuluaga and Houze 2013; Powell and Houze 2013). The combined SUR and RHI scans complete a cycle in 15 min, covering an area up to 150 km away from the radar. This radar dataset is available from 1 October 2011 through 16 January 2012. Rain rates are estimated from the S-band reflectivity, differential reflectivity, and derived specific differential phase using an algorithm from Colorado State University (CSU). The rain-rate relationships with the above three variables were derived in Thompson et al. (2015, 2018). This study uses the 1 km × 1 km S-Polka rain rates from the DYNAMO dataset at http://dynamo.fl-ext.ucar.edu/rsmas/dynamo_legacy/, which includes best-estimate rain rate that used in this study.

Rain types are classified following the algorithm of Powell et al. (2016). The algorithm uses the information on both the amplitude and spatial extent of radar reflectivity to classify rainfall into six types: deep convection, stratiform, mixed (deep convection and/or stratiform), isolated convective core, isolated convective fringe, and weak rain. Deep convective rain is identified when reflectivity exceeds 38 dBZ or when it exceeds the background reflectivity defined as the mean reflectivity of echoes within 5 km. Echoes weaker than 7 dBZ are classified as weak rain. Echoes that are not convective or weak based on the criteria above and also reside within echo objects greater than 2000 km^2 are considered stratiform. Echoes that are adjacent to deep convective cores are classified as regions of mixed convective and stratiform rainfall, based on heating profiles in such regions that contain characteristics of both convective and stratiform precipitation (e.g., Schumacher et al. 2004). Other echoes with smaller horizontal area are classified as isolated convective cores or fringe, depending on the reflectivity values. The threshold parameters used here are adjusted from Powell et al. (2016) for the 1 km × 1 km–horizontal-resolution data to best match ratios of stratiform to convective rain volume observed in disdrometer data by Thompson et al. (2015). In this study, we combine the isolated convective categories since they have a similar diurnal cycle. The diurnal cycle of presumed rainfall from weak rain is also not presented as it only contributes to less than 1% of total rain.

b. DYNAMO gridded dataset

This study uses CSU-DYNAMO upper-air and surface gridded analysis version 3b data (Ciesielski et al. 2014), which combines several observational datasets including soundings, satellite data, and European Centre for Medium-Range Weather Forecasts operational analysis to generate 3-hourly, 1° × 1° data with a vertical resolution of 25 hPa from 1 October 2011 to 31 December 2011. Further details on the gridded dataset are provided by Ciesielski et al. (2014) and Johnson et al. (2015). This dataset provides the diurnal variability of large-scale atmospheric profiles during the DYNAMO period, which allows us to examine how the radar-detected diurnal rainfall and large-scale atmospheric conditions relate to each other. This gridded dataset also provides derived variables that are not available from a single station's rawinsonde data such as vertical velocity, and apparent heating and drying. We have also repeated the analysis using version 3a of this dataset, which was generated by using observations only. The main conclusions are insensitive to the selection of these two versions, but the mean spatial patterns of the derived variables that were not directly observed (e.g., pressure velocity) showed a better agreement with reanalyses products using version 3b (see also Hannah et al. 2016).

TABLE 1. Dates of the MJO enhanced and suppressed phases over S-Polka and R/V *Revelle* during October 2011–January 2012.

Enhanced (at S-Polka)	Suppressed (at S-Polka)	Enhanced (at *Revelle*)	Suppressed (at *Revelle*)
	3–14 Oct		6–17 Oct
20–30 Oct	4–16 Nov	22–30 Oct	6–19 Nov
20 Nov–1 Dec	5–9 Dec	22 Nov–2 Dec	6–8 Dec
14–22 Dec	26 Dec–8 Jan	17–25 Dec	28 Dec–1 Jan

c. *R/V* Revelle *air–sea flux data*

The research vessel R/V *Revelle*, located east of the S-Polka at around 0.10°N, 80.50°E, collected surface and ocean subsurface thermodynamic variables during DYNAMO. This dataset provides surface fluxes at 10-min intervals during 3–22 September, 1–30 October, 8 November–8 December, and 17 December–1 January, allowing us to examine the potential role of air–sea interactions in driving the diurnal cycle of rainfall.

d. *MJO identification*

MJO convective events are identified using daily, $2.5° \times 2.5°$ outgoing longwave radiation (OLR; Liebmann and Smith 1996) filtered for the MJO spatiotemporal frequency band (20–100 days and eastward zonal wavenumbers 1–5). Threshold values for enhanced and suppressed MJO convection are determined as the lower and upper 15th percentiles of the filtered OLR anomaly from 15°N to 15°S globally during October through January 1979–2015, which is around $\pm 8\,\mathrm{W\,m^{-2}}$ (Sakaeda et al. 2017; Dias et al. 2017). The MJO-filtered OLR anomaly is then averaged over a 5° box around S-Polka (2.5°S–2.5°N, 70°–75°E). When this MJO-filtered OLR anomaly is below the lower-15th-percentile threshold value and above the upper-15th-percentile threshold value, S-Polka is determined to be within the envelope of MJO enhanced or suppressed convection, respectively. This method identified 32 days of MJO enhanced and 44 days of MJO suppressed phases. The specific dates of the MJO enhanced and suppressed phases are listed in Table 1. The identified dates generally agree with MJO dates identified by other studies (e.g., Yoneyama et al. 2013; Johnson and Ciesielski 2013; DePasquale et al. 2014; Ruppert and Johnson 2015; Xu and Rutledge 2015; Kim et al. 2018).

To identify MJO events at *Revelle*, the same method was repeated using MJO-filtered OLR averaged around the location of the *Revelle* (2.5°S–2.5°N, 77.5°–82.5°E). By slightly shifting the location eastward of S-Polka, the identified MJO events are also shifted later by a few days than at S-Polka. The included dates of MJO events to examine air–sea fluxes are also limited by the availability of the measurements at the *Revelle*. The MJO events that are used to composite the *Revelle* surface flux measurements are also summarized in Table 1.

All statistical significance and error bars in this study are calculated by using a 1000-iteration bootstrap resampling test and 95% confidence level. To bootstrap, days that are used to calculate a probability or composite value are resampled with replacement.

3. Results

Figure 1 shows daily time series of total and MJO-filtered OLR anomalies averaged around the S-Polka location (2.5°S–2.5°N, 70°–75°E) and S-Polka area-averaged rain rates. The periods of enhanced and suppressed MJO phases are indicated by blue and pink shading (Fig. 1; see dates in Table 1). The daily rainfall variability agrees well with TRMM 3B42 data (not shown), and the comparison between the S-Polka and TRMM is further discussed in the appendix. Days with strong negative OLR anomaly (i.e., MJO enhanced phase) generally have higher rain rates that are largely attributed to increased stratiform and convective rain (Zuluaga and Houze 2013; Barnes and Houze 2013; Xu and Rutledge 2015; Powell and Houze 2015). The rest of this study examines the diurnal cycle during the identified dates of the MJO enhanced and suppressed phases. The diurnal cycle during the neutral phase of the MJO or for the entire DYNAMO period shows mixed characteristics of the enhanced and suppressed phases, and so will not be discussed in detail.

a. *The diurnal cycle by rainfall type*

Figures 2a and 2b show hourly mean area-averaged diurnal rain rate from S-Polka by rain type during the MJO enhanced and suppressed phases. The daily mean and diurnal amplitude of total rain (black) is stronger within the MJO enhanced than the suppressed phase (note the scale difference on the vertical axes). Within the MJO enhanced phase, all rain types generally peak around 0600 LST, while stratiform peaks a few hours later. The total rain is partitioned into primarily deep convection, followed by mixed, then stratiform, and finally isolated convective rain. In contrast, Fig. 2b shows a double peak with rainfall maxima at 0300 and 1800 LST, this time made up primarily of convective and isolated rain types. This bimodal peak is not driven primarily by the rainfall variability associated with solar

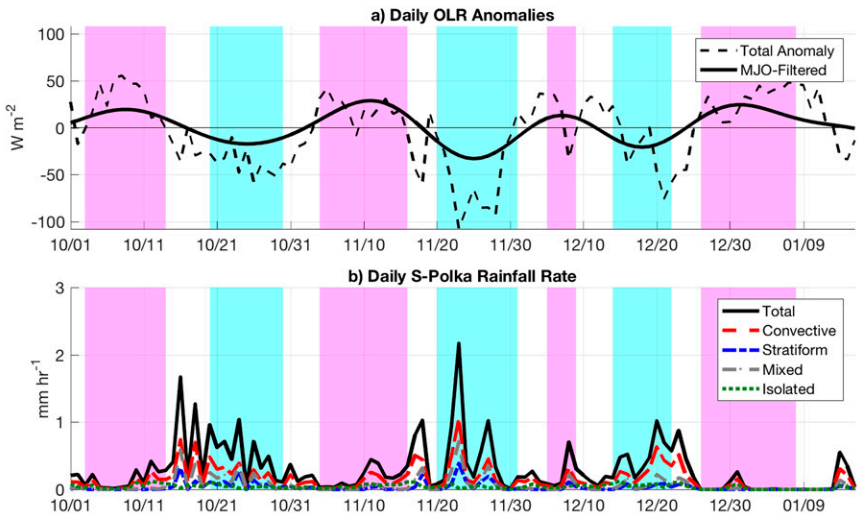

FIG. 1. Daily time series of (a) total and MJO-filtered OLR anomalies averaged over 2.5°S–2.5°N, 70°–75°E and (b) area-weighted rainfall rate (mm h^{-1}) estimated from the S-Polka radar averaged over the coverage area by rain type. In (b), black solid line shows total, red dashed line shows deep convective, blue dashed line shows stratiform, gray dotted–dashed line shows convective and stratiform mixed, and green dotted line shows isolated convective rain. Light blue and pink shading indicate dates identified as the MJO enhanced and suppressed phases, respectively.

semidiurnal tide shown by Kohyama and Wallace (2016), who document that such rainfall rates are less than 10% of the values shown in Fig. 2b. In addition, the bimodal peaks in Fig. 2b are not 12 h apart. The secondary 1800 LST peak in Fig. 2b is often less prominent in some earlier studies that used TRMM 3B42 (Oh et al. 2012; Rauniyar and Walsh 2011; Sakaeda et al. 2017), likely due to sampling issues (see appendix). In

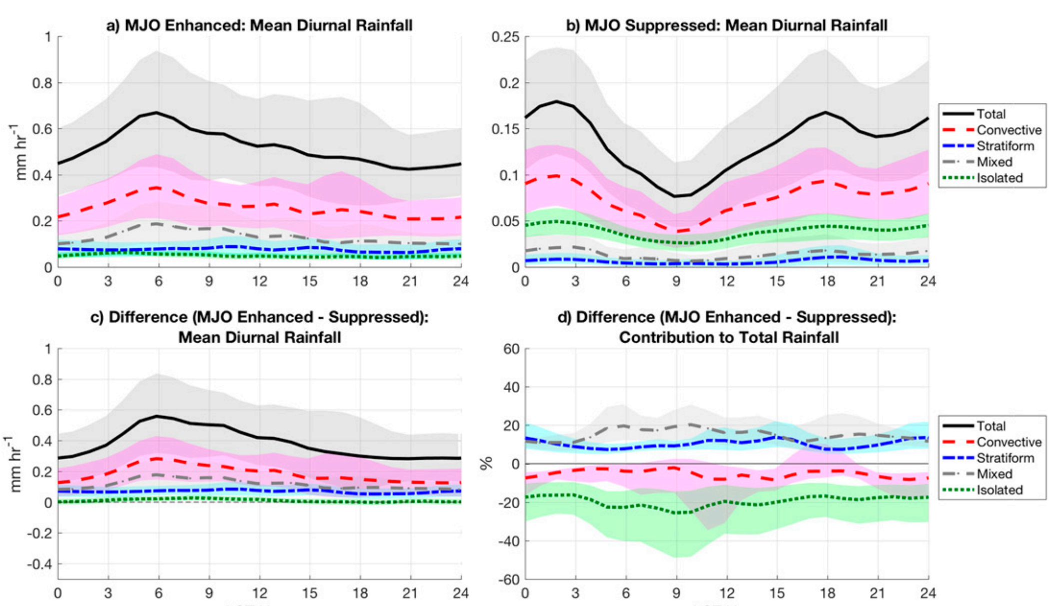

FIG. 2. Hourly mean area-weighted rain rate from S-Polka during (a) the MJO enhanced and (b) suppressed phases by rain type: total (black solid), deep convective (red dashed), stratiform (blue dashed), convective–stratiform mixed (gray dotted–dashed), and isolated (green dotted) rain. (c) Mean hourly difference between the MJO enhanced and suppressed phases. (d) Hourly difference of the percentage contribution by each rain type to the total rain between the MJO enhanced and suppressed phases. Hourly values are all smoothed by using a 1–2–1 triangular smoothing function.

Fig. 2c, the difference in the mean rain rate between the MJO enhanced and suppressed phase shows a statistically significant increase in all rain types within the MJO enhanced phase except for isolated convective rain. Figure 2d shows the difference in the percentage of contribution of each rain type to total rain between the MJO enhanced and suppressed phases. Stratiform and mixed contribute more within the MJO enhanced phase, while isolated convective rain contributes more within the suppressed phase, in agreement with previous studies (Zuluaga and Houze 2013; Barnes and Houze 2013; Xu and Rutledge 2015; Powell and Houze 2015). However, there is no significant diurnal variability in the contributions by each rain type between the MJO phases. This result indicates that the phase of the diurnal cycle of all rain types is modulated by the MJO in a similar manner, and the contribution of each rain type to total rain changes between the MJO phases at the similar rate at all hours of the day. For the rest of the study, deep convection and mixed rain types are combined since they display similar diurnal characteristics.

1) Distribution of diurnal range and peak hour

Figure 3 shows the probability distribution of the diurnal range and peak hour of each rain type from S-Polka during the MJO enhanced (blue) and suppressed (red) phases. The dots on the horizontal axis show the mean values during the MJO phases. The diurnal range is the difference between the maximum and minimum rainfall rate at each day and the diurnal peak hour indicates the local solar time (LST) when the maximum rainfall rate occurs during each day. We have also calculated the amplitude of the diurnal harmonic as done in Sakaeda et al. (2017) and obtained consistent results to using the diurnal range (not shown). The rain rates are averaged hourly and regridded to a $0.25° \times 0.25°$ grids to match the horizontal resolution of TRMM 3B42 that has been commonly used in previous studies to examine the diurnal cycle of rain (e.g., Yang and Smith 2006; Kikuchi and Wang 2008; Peatman et al. 2015). The data are regridded by applying weighted averaging, so that the total area-integrated rainfall is conserved.

The diurnal range of total rain increases from the MJO suppressed to the enhanced phase because of the increased diurnal range in all rain types except isolated convective rain. Within the MJO enhanced phase, all rain types tend to peak most frequently around 0400–0600 LST. In comparison, within the MJO suppressed phase, the probability of the diurnal peak of all rain types tends to decrease in the later morning hours (0600–0900 LST), while the probability increases slightly between 1800 and 0300 LST. Stratiform rain within the suppressed phase also shows a more distinct bimodal peak at around 0200–0400 and 1700–2000 LST. The distribution curves of the diurnal peak hour are not completely different between the MJO enhanced and suppressed phases, but they exhibit some shift in the overall pattern. The main differences between the MJO enhanced and suppressed phases are that the morning peak tends to occur earlier and a peak occurs more frequently in the late afternoon and evening within the MJO suppressed phase.

To better understand the diurnal distribution of rain rate, Fig. 4 shows the hourly probability distribution of the 15-min rain rate by rain type. The left column of Fig. 4 is the probability distribution of rain rate from all hours of the day (i.e., the all-hour distribution). The probability is only shown for nonzero rain rates, but the distribution integrates to 100% when the probability of no rain is included. The center and right columns show the anomalous probability distribution from the all-hour distribution at each hour of the day, calculated following Sakaeda et al. (2017). Positive anomalies indicate that the probability of the rain rate at that hour is higher than other hours of the day. Black and gray crosses show points where the values are statistically significantly different from zero at the 95% and 80% confidence levels.

Within the MJO enhanced phase, isolated convective rain at all rates becomes most frequent around 0200–0600 LST (Fig. 4k). Deep convective and mixed rain is most frequent around 0400–0900 LST (Fig. 4e). The probabilities of isolated and deep convective rain suggest that some isolated convection develops into deeper convection and intensifies in the morning until around 0600–0800 LST. Although the confidence level is lower, relatively strong stratiform rain (above $1\,\mathrm{mm\,h^{-1}}$) is more frequent around 0600–1200 LST (Fig. 4h), suggesting the transition of deep convection into stratiform. The stratiform rain then weakens toward the afternoon until around 1500 LST.

Within the MJO suppressed phase, all rain types show a peak in the early morning hours (0000–0300 LST) and another weaker secondary peak around 1800–2100 LST. The probability of isolated convective rain is nearly equal between the MJO enhanced and suppressed phases, although the timing of the occurrence is different (Figs. 4j–l). The intensification of convective rain or upscale growth of convective to stratiform rain is not apparent during the MJO suppressed phase, suggesting a shorter life cycle and less organization of clouds. These results suggest that, in the MJO suppressed phase, rainfall that initiates in the afternoon does not continuously intensify throughout the night before peaking in the morning. The rain that initiates in the afternoon appears to dissipate before redeveloping

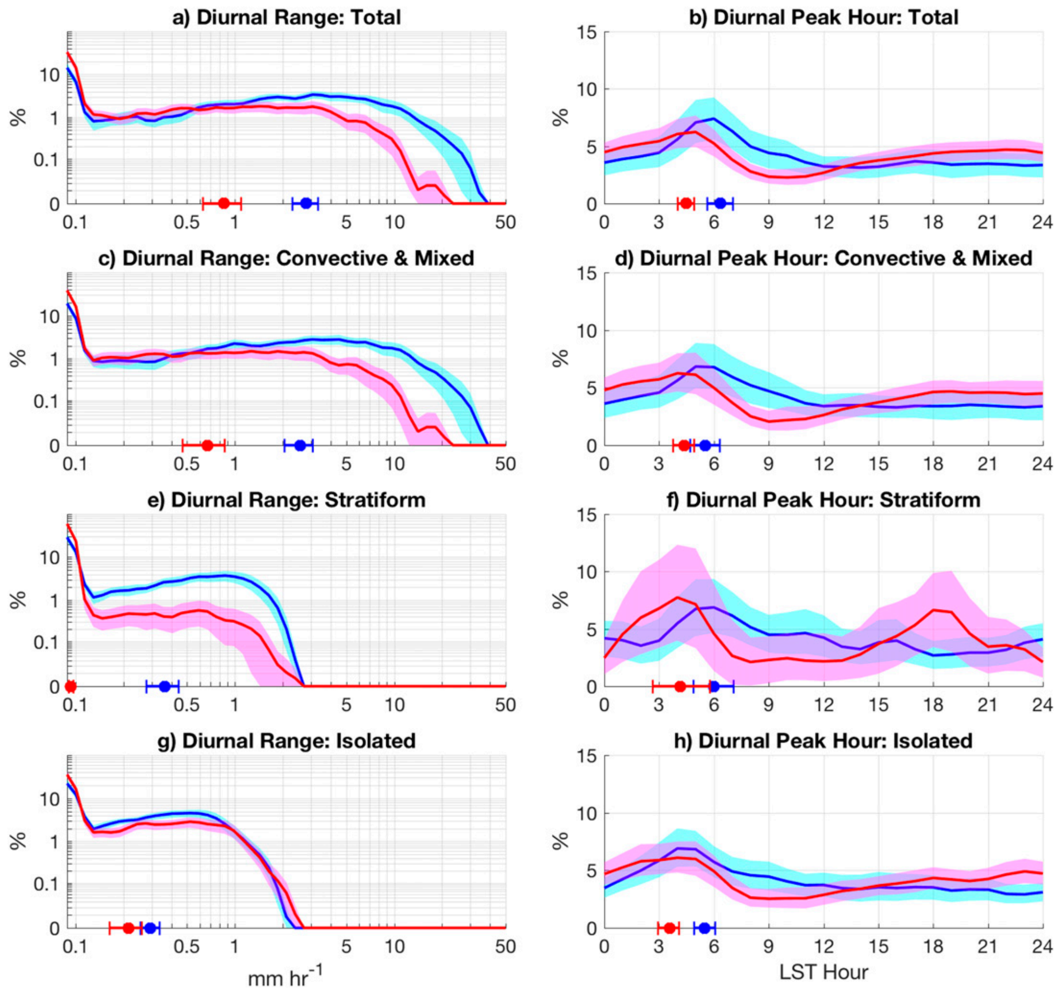

FIG. 3. Probability distribution function (%) of (left) diurnal range of rainfall rate (mm h^{-1}) and (right) local hour of diurnal peak rainfall for (a),(b) total; (c),(d) sum of convective and uncertain; (e),(f) stratiform; and (g),(h) isolated rain types from hourly S-Polka data at 0.25° horizontal resolution. Blue and red lines show the distribution during the MJO enhanced and suppressed phases, respectively. Dots on the horizontal axis represent mean values. Error bars show the 95% confidence interval. The distributions are all smoothed using a 1–2–1 triangular smoothing function.

after midnight. Within the MJO enhanced phase, cloud systems instead seem to begin developing or intensifying after midnight and exhibit a longer lifetime.

2) FACTORS CONTRIBUTING TO THE DIURNAL CYCLE OF RAINFALL

The diurnal cycle of rain over an area domain can be influenced by two factors: diurnal changes in the fraction of raining area and the intensity of rain. Figures 5a and 5b show the mean hourly time series of raining areal coverage (note the scale difference on the vertical axes), and Figs. 5c and 5d show the conditional rain rate over the radar domain during the MJO enhanced and suppressed phases. Raining areal coverage represents the fraction of the radar area that is raining. Conditional rain rate is calculated as the mean rain rate within the raining area, providing better estimates of rain intensity. Weak rain is excluded from both estimates because of its frequent appearance and small contribution to the diurnal cycle of total rainfall.

Daily mean areal coverage of all rain types is greater within the MJO enhanced phase as shown in previous studies (e.g., Chen et al. 1996; Riley et al. 2011; Barnes and Houze 2013; Powell and Houze 2013; Xu et al. 2015), but the conditional rain rates do not vary much between the MJO phases, except for the slightly stronger deep convective and mixed rainfall during the MJO suppressed phase. The conditional probability distributions of rain rates (i.e., rain-rate probability normalized by the number of raining points, instead of all data

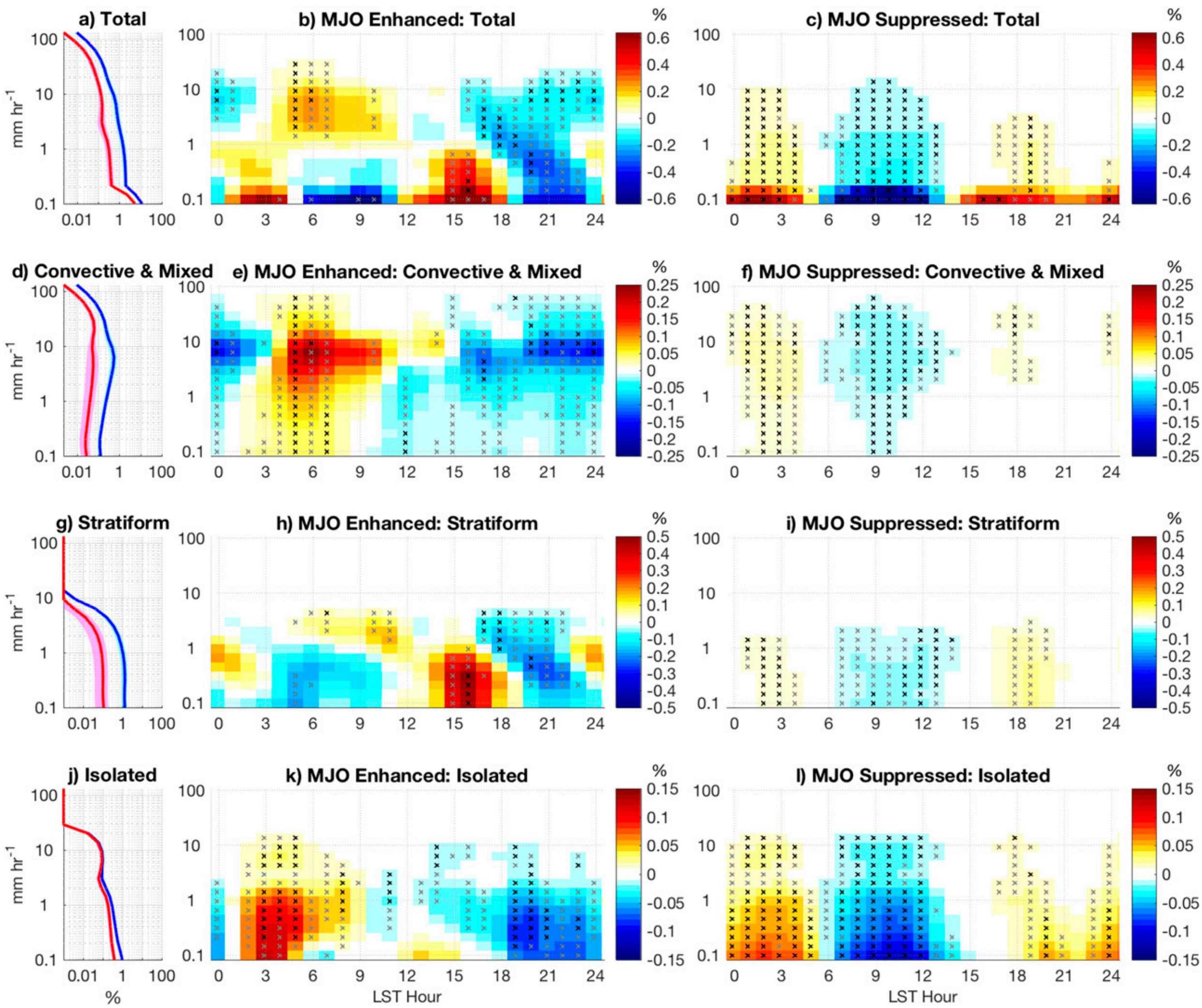

FIG. 4. (left) Probability distribution function (%) of S-Polka rain rate from all hours of the day. The distribution does not show the probability of no rainfall, but integrates to 100% when the probability of no rain is included. Blue and red lines show the distribution during the MJO enhanced and suppressed phases, respectively. (center),(right) The anomalous hourly probability (%) from the distribution shown in the left column. Anomalous hourly probability distribution within the (b),(e),(h),(k) MJO enhanced phase and (c),(f),(i),(l) suppressed phase. Black crosses indicate that the anomaly is significantly different from zero at the 95% confidence level, and gray crosses indicate the 80% confidence level.(top)–(bottom) Different rain types: total, convective andmixed, stratiform, and isolated rain, respectively. The probabilities are calculated using 15-min rain rates from S-Polka. The distributions are all smoothed using a 1–2–1 triangular smoothing function in one dimension for the left column and in two dimensions for the center and right columns.

points as in Fig. 4) also did not show significant variability between the MJO phases (not shown). These results confirm that total rain increases within the MJO enhanced phase because of increased coverage in the raining area. Although the mean conditional rainfall rates do not vary much as a function of the MJO phase, the heights of echoes above some thresholds (e.g., 0 and 20 dBZ) increase within the MJO enhanced phase (not shown), consistent with previous studies (Powell and Houze 2013; Xu et al. 2015). Our results here suggest that the increase in echo-top heights is not representative of changes in mean rainfall intensity. The areal coverage of stratiform rain increases the most from the suppressed to enhanced MJO phase (Figs. 4a,b), but its contribution to total area-averaged rain is still small (Fig. 2) because the intensity of stratiform rain is relatively weak (Fig. 4 and Figs. 5c,d).

While the areal coverage does show some diurnal variability that is generally in phase with the area-averaged rain rates for most rain types (Fig. 2), the conditional rain rates do not show much diurnal variability within either MJO phase. To quantify the contribution of the raining areal coverage and conditional rain, the area-averaged rain R (Fig. 2) can be first written

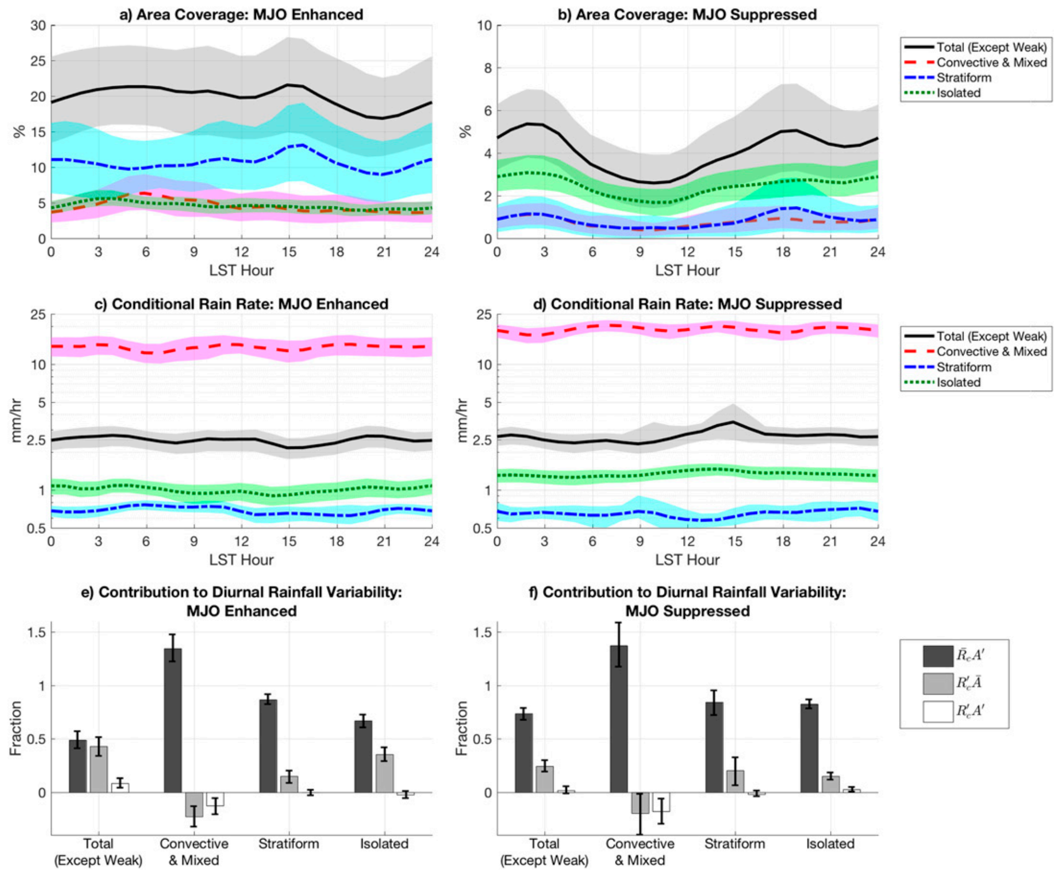

FIG. 5. Hourly mean time series of (a),(b) raining areal coverage (%) and (c),(d) conditional rain rate (mm h^{-1}) within the radar-covered region during the MJO (left) enhanced and (right) suppressed phases. Black line shows the raining areal coverage of total rain not including weak rain type, red dashed line shows deep convection and convective–stratiform mixed, blue dashed line shows stratiform, and green dotted line shows isolated convective rain. Hourly values are all smoothed by using 1–2–1 triangular smoothing function. (e),(f) Contribution of areal coverage and conditional rain rate to diurnal rainfall variability shown as the mean ratios of each term on the rhs of Eq. (3) to R'. See text for more details on how these ratios are calculated. The 95% confidence intervals are shown with shadings in (a)–(d) and with black lines in (e) and (f).

as a product of raining area fraction A_r and conditional rain rate R_c:

$$R = R_c A_r. \tag{1}$$

Each variable is then decomposed into its daily mean (overbar) and deviation from the daily mean (prime):

$$R = \overline{R} + R'. \tag{2}$$

Then, the diurnal variability of area-averaged rainfall rate R' can be represented as the sum of three terms:

$$R' = \overline{R_c} A'_r + R'_c \overline{A_r} + (R'_c A'_r)', \tag{3}$$

where the first term on the right-hand side (rhs) of Eq. (3) represents the contribution by the diurnal variability of raining area fraction, the second term represents the contribution by the diurnal variability of conditional rain rates, and the third term represents the contribution by the covarying diurnal variability of both factors.

Figures 5e and 5f show the mean fraction of each term on the rhs of Eq. (3) to R' for each rain type during the MJO phases. To eliminate points with near-zero denominator (i.e., $R' \approx 0$), we excluded the times when R' was within the upper and lower 95% confidence intervals of $\overline{R}$ for each rain type, which is equivalent to the confidence intervals shown in Fig. 2 averaged over all hours. When the mean fraction is close to one, it indicates that the term contributes dominantly to R', while near-zero or negative fractions indicate that the term only weakly contributes or opposes R'. Figures 5e and 5f clearly show that the diurnal variability of area-averaged rain R' of each rain type is primarily driven by the diurnal variability of raining areal coverage $\overline{R_c} A'_r$ during both MJO phases. An exception appears for total rain rate during the MJO enhanced phase which has more similar contributions by the areal coverage and conditional rain rate, although even in that case the areal coverage is still the primary contributor, in agreement with Nesbitt and Zipser (2003), Biasutti et al. (2012), and Sakaeda et al. (2017). The raining areal coverage fluctuates diurnally mostly due to changes in the number of raining clusters rather than the size of clusters (not shown), as shown by previous studies (Barnes and Houze 2013; Dias et al. 2017). This result does not mean that the raining clusters do not grow in size overnight as suggested by Chen and Houze (1997), but rather that while some raining clusters grow, new smaller clusters also form, maintaining the mean and probability distribution of cluster sizes, with the number of raining clusters contributing to the changes in the total areal coverage.

b. *Large-scale diurnal variability of the troposphere*

To better understand what drives the diurnal cycle of rainfall, this section examines diurnal variability of large-scale atmospheric conditions using $1^\circ \times 1^\circ$ DYNAMO gridded analysis (section 2b) and compares them with the diurnal cycle of rainfall during the two MJO phases. As discussed in section 1, diurnal rainfall variability may be due to interactions of clouds with radiation (Kraus 1963; Gray and Jacobson 1977; Randall et al. 1991; Frenkel et al. 2011) and moisture (Sui et al. 1997; Frenkel et al. 2011), air–sea interactions (Sui et al. 1997; Chen and Houze 1997; Ruppert and Johnson 2015), or large-scale atmospheric variability associated with atmospheric tides (Lindzen 1978; Ueyama and Deser 2008; Kohyama and Wallace 2016). We will assess the relevance of those proposed mechanisms by examining the diurnal cycle of atmospheric temperature, moisture, circulation, air–sea fluxes, and apparent heating and drying terms defined by Yanai et al. (1973). The DYNAMO gridded analysis data include estimates of apparent heating Q_1 and apparent drying Q_2 as the residuals of the dry static energy ($s = c_pT + gz$) and latent heat energy (qL_v) budget, where c_p is the specific heat of dry air at constant pressure, T is the temperature, z is the geopotential height, q is the water vapor mixing ratio, and L_v is the latent heat of vaporization.

As shown in Yanai et al. (1973), Q_1 can be expressed as

$$Q_1 = Q_R + L_v(c - e) - \frac{\partial}{\partial p}s^*\omega^*, \tag{4}$$

representing the sum of radiative heating Q_R, diabatic heating associated with condensation c and evaporation e, and vertical eddy flux convergence of dry static energy where ω is pressure velocity and asterisks indicate scales unresolved by $1^\circ \times 1^\circ$ grids (i.e., eddies).

Variable Q_2 represents the sum of moisture sinks and sources by condensation and evaporation and the vertical eddy flux convergence of moisture:

$$Q_2 = L_v(c - e) + L_v\frac{\partial}{\partial p}q^*\omega^*. \tag{5}$$

If the changes in the diurnal cycle of rainfall are driven by radiation as suggested by Kraus (1963) and Randall et al. (1991), the diurnal cycle of Q_1 and rainfall should vary consistently with the MJO phases. Likewise, if the moisture variability drives the diurnal cycle of rainfall, and if clouds themselves drive the moisture variability, q and Q_2 must also vary consistently with the rainfall.

The vertical profiles in the left column of Fig. 6 show mean potential temperature, water vapor mixing ratio, and pressure velocity averaged over all available dates and hours during DYNAMO (i.e., the mean vertical profiles) around the location of S-Polka (2°S–1°N, 71°–75°E). The shaded time–pressure diagrams in the same column are 3-hourly anomalies of these variables from their daily mean values, showing the mean diurnal cycle during the DYNAMO period. The center and right columns of Fig. 6 show the same daily profiles and 3-hourly anomalies for the MJO phases after removing their mean over the entire DYNAMO period (i.e., anomalies from the left column of Fig. 6). The anomalous vertical profiles reveal well-known signals associated with convective regimes (e.g., Kiladis et al. 2005; Johnson and Ciesielski 2013), with a more moist environment (Fig. 6e) and enhanced rising motion (negative ω, represented by blue shading in Fig. 6h). A slight cooling at the lowest levels with warmth in the upper troposphere (Fig. 6b) also appears during the MJO enhanced phase, with the opposite anomalies seen during the suppressed phase.

Figure 6a depicts an overall colder troposphere in the morning and warm anomalies in the afternoon, with the largest signals at the surface and a secondary maximum at around 250 hPa. As is well known, the surface signal slightly lags the diurnal cycle of solar radiation, and the upper-tropospheric temperature in turn lags the surface temperature, peaking in the late afternoon. Within the MJO enhanced convection, potential temperature shows an anomalous cold signal near the top of deep clouds (i.e., 200–400 hPa) in the morning, which is mostly driven by Q_1 (Fig. 7b). This less thermally stable upper troposphere might encourage the development of deeper clouds in the morning, as suggested by Kraus (1963) and Randall et al. (1991). However, it is unclear whether this is a cause or effect of rainfall and high clouds.

Surface temperature variability reflects a diurnal SST cycle that has higher amplitude of variability within the MJO suppressed phase (Sui et al. 1997; Johnson et al. 1999;

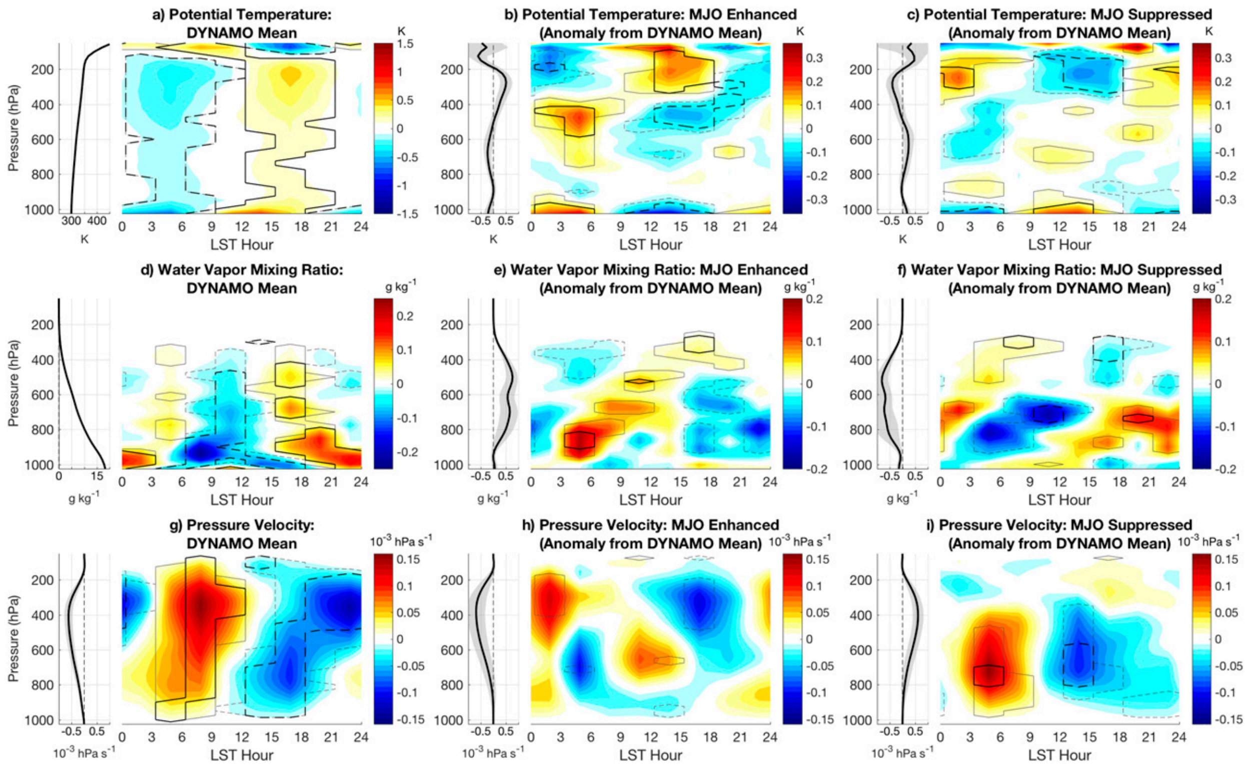

FIG. 6. (left) Black line in the left plot of each panel shows the vertical profiles of daily mean (a) potential temperature (K), (d) water vapor mixing ratio (g kg^{-1}), and (g) pressure velocity (hPa s^{-1}) averaged over the S-Polka radar region (2°S–1°N, 71°–75°E) and over the entire DYNAMO period. Shading in the right plot of each panel shows the time–pressure diagrams of 3-hourly anomalies of those variables from their daily mean values. (center),(right) As in the left column, but averaged during the MJO (b),(e),(h) enhanced and (c),(f),(i) suppressed phases after removing the mean over the entire DYNAMO period. The plotted values are smoothed in the vertical direction using a 1–2–1 triangular smoothing function. Black solid and dashed contours outline the positive and negative anomalies that are statistically significantly different from zero at the 95% confidence level and thin gray contours show the 80% confidence level.

Matthews et al. 2014; Ruppert and Johnson 2015). Using a cloud-resolving model, Ruppert and Johnson (2016) showed that this diurnal SST warming and associated surface fluxes trigger nonprecipitating cumulus clouds around noon, followed by precipitating clouds during late afternoon. In Fig. 7c, this near-surface warming is driven by Q_1, which is stronger before 1200 LST within the MJO suppressed phase (Figs. 7b,c), indicating a contribution of heat flux from the ocean or through radiation. Measurements from the R/V *Revelle* show that surface fluxes are stronger during the MJO enhanced phase, and this is primarily due to increased wind speed (not shown). The sum of sensible and latent heat flux peaks in the afternoon during both MJO phases (Fig. 8). This indicates that surface fluxes alone cannot explain the existence and nonexistence of afternoon rainfall peak during the MJO suppressed and enhanced phases. Therefore, the thermal destabilization of lower troposphere associated with radiative heating rather than air–sea fluxes perhaps plays a primary role in triggering the afternoon rainfall during the MJO suppressed phase, but not during the enhanced phase.

On average during the entire DYNAMO period (Fig. 6d), diurnal variability of water vapor mixing ratio shows a more pronounced 24-h cycle in the lower troposphere with a nocturnal peak (below 850 hPa), while a semidiurnal cycle appears in the mid- to upper troposphere with peaks at around 0500 and 1700 LST. This semidiurnal cycle of water vapor mixing ratio could be associated with the semidiurnal solar tide, as recently documented by Kohyama and Wallace (2016), while the lower-tropospheric water vapor is driven by the diurnal cycle of air–sea fluxes (Ruppert and Johnson 2015). Within the MJO suppressed phase (Fig. 6f), moistening begins near the surface around noon then gradually builds upward, reaching 800–600 hPa at around midnight. In contrast, within the MJO enhanced phase, lower-tropospheric moisture begins to build up from early morning into early afternoon (Fig. 6e). This lag in lower-tropospheric moisture is consistent with the delayed

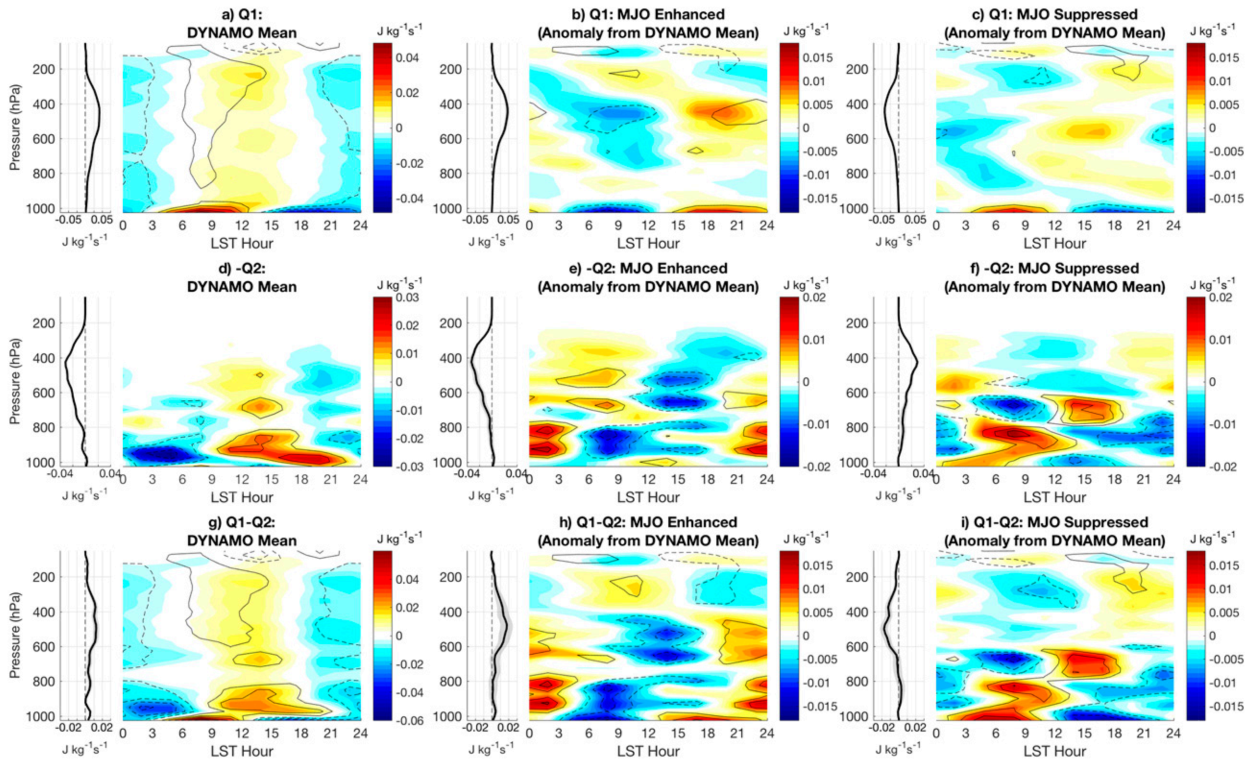

FIG. 7. As in Fig. 6, but showing (top) Q_1, (middle) $-Q_2$, and (bottom) $Q_1 - Q_2$. Black contours show the time tendency of (a)–(c) dry static energy ($\partial s/\partial t$), (d)–(f) latent heat energy ($\partial L_v q/\partial t$), and (g)–(i) moist static energy ($\partial m/\partial t$) at intervals of (left) 0.01 and (center), (right) 0.005 J kg^{-1} s^{-1}, where solid (dashed) lines indicate positive (negative) values.

morning rainfall within the MJO enhanced phase. The earlier morning peak within the MJO suppressed phase (0000–0300 LST) is consistent with the earlier buildup of moisture that peaks around midnight, while the later peak within the MJO enhanced phase (0400–0800 LST) is consistent with the delayed buildup of moisture that peaks in late morning. The consistent variability between the lower-tropospheric (700–1000 hPa) moisture and the timing of early morning rainfall peak supports the importance of moisture buildup during the prior evening (Sui et al. 1997; Frenkel et al. 2011).

The diurnal variability of latent heat energy $L_v q'$ or moisture is driven by advection and Q_2':

$$L_v\frac{\partial q'}{\partial t} = -L_v\left(\overline{\mathbf{v}}\cdot\nabla q' + \overline{\omega}\frac{\partial q'}{\partial p} + \mathbf{v}'\cdot\nabla\overline{q} + \omega'\frac{\partial\overline{q}}{\partial p}\right) - Q_2', \tag{6}$$

where $\mathbf{v}$ denotes horizontal wind on pressure surfaces. Figures 7d–f show that $L_v\partial q'/\partial t$ is almost entirely driven by Q_2' as the contours ($L_v\partial q'/\partial t$) and shadings ($-Q_2'$) coincide with the same magnitude. These figures plot the negative of the Q_2 term, so positive (red) anomalies indicate apparent moistening. The correlation between $L_v\partial q'/\partial t$ and $-Q_2'$ is also 0.8–0.98 between 600 and 1000 hPa (not shown). In contrast, Ruppert and Johnson (2016) showed that, within the MJO suppressed phase, column-integrated moisture increases in the afternoon hours by the vertical advection of moisture by anomalous large-scale ascent. While vertical advection can become important in the midtroposphere and impact the column-integrated moisture budget (not shown), it does not dominate the diurnal moisture variability in the lower troposphere.

The sum of Q_1 and $-Q_2$ cancels out $L_v(c - e)$ (Eq. 7) and drives moist static energy $m = s + L_v q$ (Eq. 8):

$$Q_1 - Q_2 = Q_R - \frac{\partial}{\partial p}s^*\omega^* - L_v\frac{\partial}{\partial p}q^*\omega^* \quad \text{and} \tag{7}$$

$$\frac{\partial m'}{\partial t} = -\left(\overline{\mathbf{v}}\cdot m' + \overline{\omega}\frac{\partial m'}{\partial p} + \mathbf{v}'\cdot\overline{m} + \omega'\frac{\partial\overline{m}}{\partial p}\right) + (Q_1' - Q_2'). \tag{8}$$

The anomalous moistening around midnight to early morning occurring within the MJO enhanced phase (Fig. 7e) leads to a positive moisture anomaly in the morning hours (Fig. 6e). The appearance of a similar pattern between Q_2 (Figs. 7e,f) and $Q_1 - Q_2$ (Figs. 7h,i) indicates that the diurnal variability of lower-tropospheric moisture ($L_v\partial q'/\partial t$) is driven by the eddy

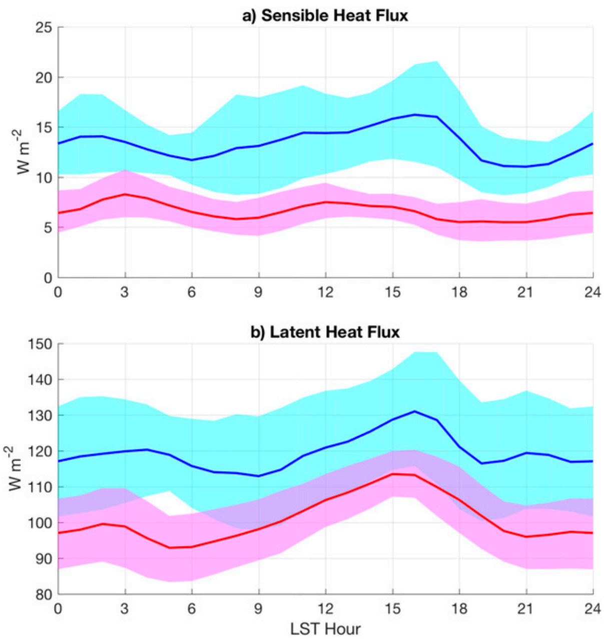

FIG. 8. Hourly time series of mean (a) sensible heat flux and (b) latent heat flux, measured at the R/V *Revelle* during the MJO enhanced (blue) and suppressed (red) phases around the location of the ship (2.5°S–2.5°N, 77.5°–82.5°E). The hourly time series are all smoothed by using a 1–2–1 triangular smoothing function. The shading shows the 95% confidence interval.

flux convergence [second term in Eq. (5)], since the evaporation/condensation term is cancelled in $Q_1 - Q_2$. Within the MJO suppressed phase, more cumulus and convective clouds are triggered in the afternoon than in the MJO enhanced phase, which is thought to lead to stronger moistening at those hours (Johnson et al. 1999; Benedict and Randall 2007; Waite and Khouider 2010; Frenkel et al. 2011; Powell and Houze 2013). The moistening also extends up to 600 hPa during the MJO suppressed phase in the afternoon, which can likely be ascribed to more abundant cumulus congestus clouds (Johnson et al. 1999; Ruppert and Johnson 2015) that are not necessarily captured by S-Polka if they are not precipitating. In contrast, during the MJO enhanced phase, the lack of the afternoon triggering of cumulus congestus clouds could potentially lead to a delayed moistening of the lower troposphere and peak rainfall in the morning hours. More abundant total moisture in the troposphere and a larger horizontal scale of raining clusters within the MJO enhanced phase may also lead to slower decay rate of clouds and rainfall that peak in the late morning hours by reducing the entrainment of dry air into clouds. Surface fluxes cannot explain these differences in the diurnal anomaly of lower-tropospheric moisture because, in both phases of the MJO, surface latent heat fluxes peak in the afternoon (Fig. 8b).

The vertical ascent is reduced (i.e., there is anomalous descent) during the morning hours on average (Fig. 6g), even though rainfall tends to peak then. It turns out that this anomalous descent in the morning is dominated by those days with weak or no rain (not shown). A similar result was obtained by Ueyama and Deser (2008), who found that the near-surface divergence also peaks around 0700 LST at the equator over the Pacific basin using the buoy wind data. This is consistent with anomalous descent in the morning hours based on mass conservation, despite the fact that this is also the time of peak rainfall over that region (Yang and Slingo 2001; Sakaeda et al. 2017). The enhanced large-scale ascent favors the development of deep convective clouds and associated rainfall by sustaining the updraft within clouds. However, the mismatch between the diurnal cycle of rainfall and vertical motion suggests that the diurnal cycle of the large-scale atmospheric circulation, which is associated with winds that are primarily driven by the diurnal variability of pressure gradient force (Ueyama and Deser 2008), is not the dominant driver of the diurnal cycle of rainfall.

Although the significance level is weak, within the MJO enhanced phase, the diurnal variability of pressure velocity shows anomalous ascent between 0300 and 0600 LST at around 600–800 hPa and in the upper troposphere (200–400 hPa) at around 1500–1800 LST. These signals are consistent with the timing of deep convection and stratiform rain (Figs. 4e,h), suggesting that these signals in the vertical motion appear as a consequence of the diurnal cycle of rainfall. During the MJO suppressed phase, vertical motion does not show morning and afternoon bimodal peaks as is apparent in the rainfall signal (Fig. 2b). This again suggests that the large-scale atmospheric circulation associated with tides is not the main driver of the diurnal cycle of rainfall, although the enhanced ascent in the afternoon could contribute to the afternoon rainfall within the MJO suppressed phase.

4. Summary and conclusions

This study examines the diurnal cycle of rainfall by rain types within the enhanced and suppressed MJO convective envelopes during DYNAMO, and associated variability in large-scale atmospheric conditions, using high-spatial- and -temporal-resolution rain-rate estimates from the S-Polka radar along with the gridded dataset provided by Ciesielski et al. (2014). Previous studies have found that, over the tropical ocean, the amplitude of the diurnal cycle increases and the peak diurnal rainfall tends to occur during the later morning hours within the convectively enhanced envelopes of the MJO when compared to the suppressed envelope

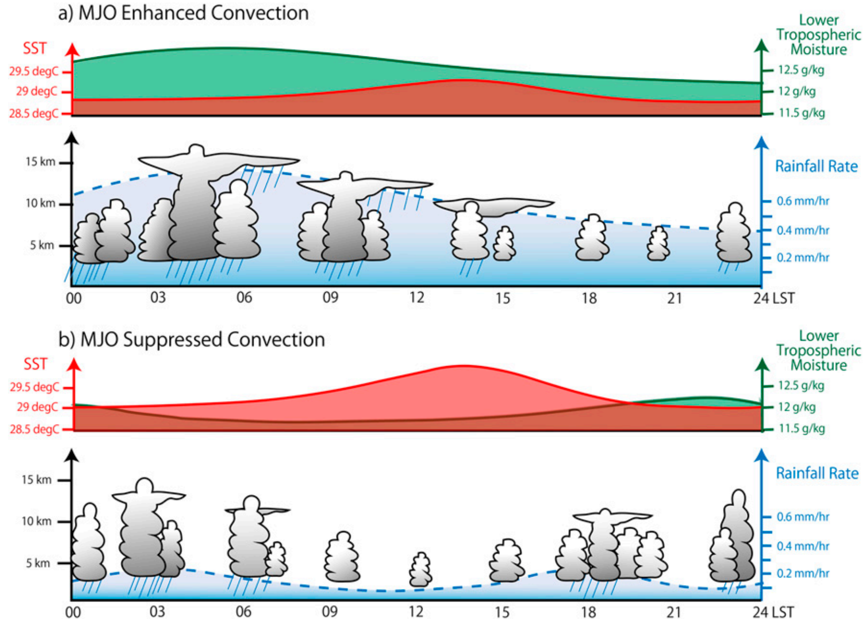

FIG. 9. Schematic of the diurnal cycle of rainfall, clouds, lower-tropospheric moisture, and SST during the MJO (a) enhanced and (b) suppressed phases during the DYNAMO field campaign. Green and red shading at the top of each panel represent the diurnal variability of lower-tropospheric (averaged from 700 to 1000 hPa) water vapor mixing ratio and SST. Blue lines at the bottom of each panel represent the diurnal variability of total rainfall over the area covered by the S-Polka radar. Tall clouds indicate convective and accompanying wide thin clouds represent stratiform–anvil clouds. Other shallower clouds represent those associated with isolated convective rain.

(Oh et al. 2012; Rauniyar and Walsh 2011; Sakaeda et al. 2017). This signal has been attributed to an increase in rain associated with stratiform cloud development that follows deep convection (Sakaeda et al. 2017). To follow up on the findings of previous studies, we used the radar rain-type classification algorithm developed by Powell et al. (2016) to examine the diurnal cycle of isolated shallow convective elements, deeper convection, and broader stratiform regions.

We find that the increase in the diurnal range of rainfall from the MJO suppressed to enhanced phase is not driven by increased precipitation from all rainfall types, but is primarily due to deep convective and stratiform rain, with relatively little change in isolated convective rain (Fig. 3). Morning rainfall tends to peak at later hours within the MJO enhanced compared to the suppressed phase (i.e., 0400–0600 vs 0000–0300 LST), consistent with previous studies (Oh et al. 2012; Rauniyar and Walsh 2011; Sakaeda et al. 2017). An afternoon rainfall peak is also observed during the MJO suppressed phase, in agreement with Sui et al. (1997), Chen and Houze (1997), Johnson et al. (1999), and Ruppert and Johnson (2015). The afternoon peak during the MJO suppressed phase is often not captured by previous studies that used satellite-based rainfall and cloudiness data (Tian et al. 2006; Suzuki 2009; Oh et al. 2012; Rauniyar and Walsh 2011; Sakaeda et al. 2017) because instrumental resolution and sensitivity are not high enough to capture small-scale, light-rain events (see appendix).

Separation of rainfall types leads to a better understanding of how the timing of diurnal rainfall changes with the MJO. Figure 9 summarizes the general characteristics of the diurnal cycle of rainfall during the MJO enhanced and suppressed phases. During the MJO enhanced phase (Fig. 9a), total rainfall tends to peak around 0400–0600 LST, composed of isolated convective rain that peaks around 0300–0500 LST, with deeper convective rain peaking around 0400–0600 LST, followed by stratiform rain that peaks broadly around 0500–1000 LST (Figs. 3, 4). During the MJO suppressed phase (Fig. 9b), deep and isolated convective rain contributes to about 80% of total rain, and all rain types tend to have bimodal peaks at around 0300–0500 and 1800–2100 LST. The lack of upscale growth of deep convective to stratiform rain during the MJO suppressed phase gives rise to a shorter time lag in the peak hour of rain between rainfall types and an earlier peak in total rain during the morning. This diurnal variability of rainfall over the S-Polka domain is mostly due to changes in the areal coverage of rainfall rather than its intensity (Fig. 5). The diurnal variability of the raining areal coverage is mostly driven by the variability in the number of raining clusters rather than their size (not shown). These results do not necessarily indicate that each raining cluster does not grow in size during the day. While some raining clusters do grow in size (Chen and Houze 1997), at the same time other clusters must shrink in size, or new smaller clusters form to maintain a similar mean and distribution of cluster sizes throughout the day.

The difference in the timing of morning rainfall is associated with the diurnal variability of lower-tropospheric moisture (Figs. 6, 7). Figure 9 shows the diurnal variability of lower-tropospheric moisture and SST during the two MJO phases. During the MJO suppressed phase, when there is less large-scale convective activity, stronger solar radiative fluxes and weaker surface wind speeds allow the SST and near-surface air temperature to warm more in the afternoon (Sui et al. 1997; Johnson et al. 1999; Matthews et al. 2014; Ruppert and Johnson 2015). This higher SST and associated surface fluxes in the afternoon trigger shallow cumulus and cumulus congestus clouds that contribute to the moistening of the lower troposphere (Ruppert and Johnson 2016), yielding a peak in lower-tropospheric moisture during the late evening, followed by a peak in rainfall shortly after midnight. The nonprecipitating cumulus congestus clouds are not necessarily captured by S-Polka, but the development of isolated convective rain (i.e., moderately deep cumulonimbus) is evident in the increasing echo-top heights of isolated convective rain from late morning to afternoon (not shown). In contrast, during the MJO enhanced phase, weaker SST warming in the afternoon may lead to weaker development of cumulus congestus clouds (Johnson et al. 1999), which would in turn delay the moistening of the lower troposphere and subsequent rainfall to later morning hours.

The observed consistency between the timing of morning rainfall and lower-tropospheric moisture buildup (Figs. 6, 9) supports the importance of tropospheric relative humidity and moisture in modulating the diurnal cycle of rainfall over tropical ocean (Sui et al. 1997; Frenkel et al. 2011). Our results suggest that cumulus clouds contribute to this lower-tropospheric moisture buildup {i.e., through $L_v \nabla \cdot [\mathbf{v}^* q^* + \partial(\omega^* q^*)/\partial p]$ within Q_2}, which could occur through the nocturnal enhancement of low-level convergence within cloudy area due to differential radiative heating within cloudy and clear areas, as proposed by Gray and Jacobson (1977). Other previously proposed mechanisms of the diurnal cycle of rainfall and cloudiness (discussed in section 1) seem to apply conditionally depending on the large-scale conditions (e.g., MJO phases). For instance, the role of afternoon SST warming suggested by Chen and Houze (1997) and Ruppert and Johnson (2015) is more significant when large-scale disturbances suppress convective activity and do not appear to play a significant role during the periods of enhanced convection.

Our results suggest a feedback between clouds, radiation, and moisture that drives the diurnal cycle of rainfall and its variability within the MJO. The cloud fraction influences the incoming solar radiation reaching the surface and the strength of the afternoon SST warming, which in turn influences the triggering of cumulus clouds. The formation of such clouds affects the moistening of the lower troposphere in the evening, which then influenced the growth of clouds overnight. These potential feedbacks need to be better quantified by atmospheric thermodynamical data that resolve cloud scales, along with cloud-resolving models. Whether the relationships documented here carry over to periods or regions outside DYNAMO also needs to be tested. The feedback of the diurnal cycle onto the intraseasonal time scales and its role in MJO dynamics also remains to be quantified from observational data and will likely require further modeling studies to completely sort out.

Acknowledgments. We gratefully acknowledge support for this work through Grant NA13OAR4310165 from the Climate Program Office at NOAA. This research was performed while the first author held an NRC Research Associateship award at NOAA. We thank the three anonymous reviewers, Emily Riley-Dellaripa, and Chris Fairall for their helpful comments and discussion that led to improvements of the manuscript. We also thank Bob Rilling for his help in downloading S-Polka radar data from UCAR Earth Observing Laboratory. S. W. Powell acknowledges support from the NOAA Climate and Global Change Postdoctoral Fellowship Program, administered by UCAR's Cooperative Programs for the Advancement of Earth System Science.

APPENDIX

Comparison of S-Polka and TRMM 3B42

This section presents a comparison between the diurnal cycle of rainfall from S-Polka and TRMM 3B42, which has been commonly used to study the diurnal cycle of rainfall and its relationship with the MJO (Rauniyar and Walsh 2011; Oh et al. 2012; Peatman et al. 2014; Sakaeda et al. 2017). The comparison allows us to address whether the relationship between the diurnal cycle of rainfall and the MJO we observe can be generalized beyond the limited space and time sampling

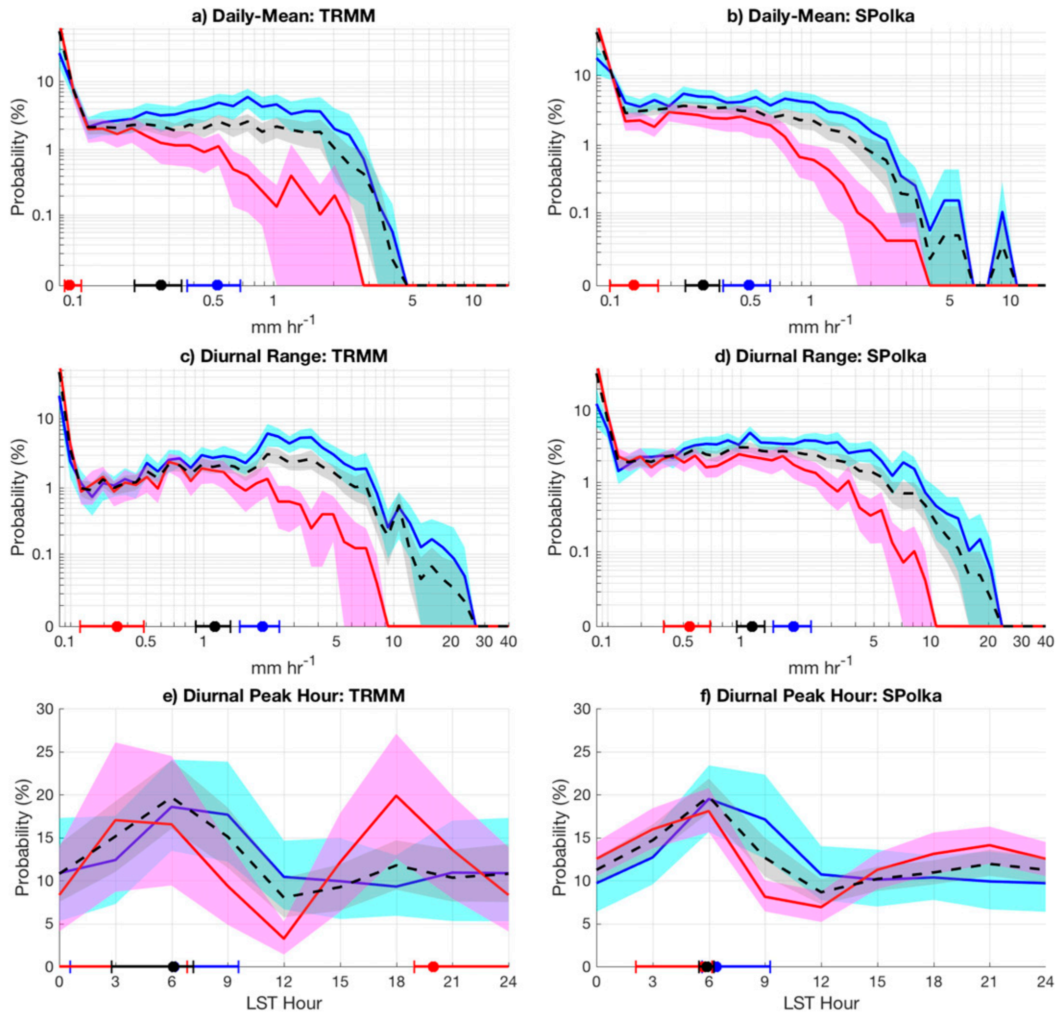

FIG. A1. Probability distribution (%) of (a),(b) daily mean; (c),(d) diurnal range; and (e),(f) diurnal peak hour of rain rate from (left) TRMM and (right) S-Polka. Rain rates from S-Polka are regridded to match the space and time resolution of TRMM and the distribution is calculated only using those points and days when both data are available. Blue and red lines show distributions on days within the MJO enhanced and suppressed phases, respectively, and the black dashed lines show distributions based on all days during DYNAMO. Dots on the horizontal axes show mean values. Error bars and shading show the 95% confidence intervals.

during the DYNAMO. The resolution of the S-Polka rain-rate data used in this comparison is regridded to the spatiotemporal resolution of the TRMM 3B42 data (i.e., 3-hourly averages on a 0.25° × 0.25° grid). Regridding is done using the same method as explained in section 3a(2).

Figure A1 shows the probability distributions of the daily mean, diurnal range, and diurnal peak hour of rain rate using only grid points and days where both TRMM 3B42 and S-Polka data were available. The distributions and mean values of the daily mean and diurnal range (dots along the horizontal axes) are similar between TRMM and S-Polka during the MJO enhanced phase (blue) or the entire period (black), but are lower in TRMM 3B42 during the MJO suppressed phase (red), likely in part because TRMM 3B42 tends to underestimate light rain (Huffman et al. 2007; Tabata et al. 2011). Figure A2a shows the distribution of the regridded S-Polka rain rates among points identified as raining by S-Polka but missed as nonraining by TRMM 3B42 and among points identified as raining by both S-Polka and TRMM 3B42. This shows that TRMM 3B42 not only tends to miss light rain, but it can also miss moderate rain rates (i.e., 1–5 mm h^{-1}). We speculate that some moderate rain rates are missed by TRMM 3B42 when some rain clusters were short-lived or too small in their horizontal extent to be detected by the instantaneous passages. Fig. A2b shows that TRMM

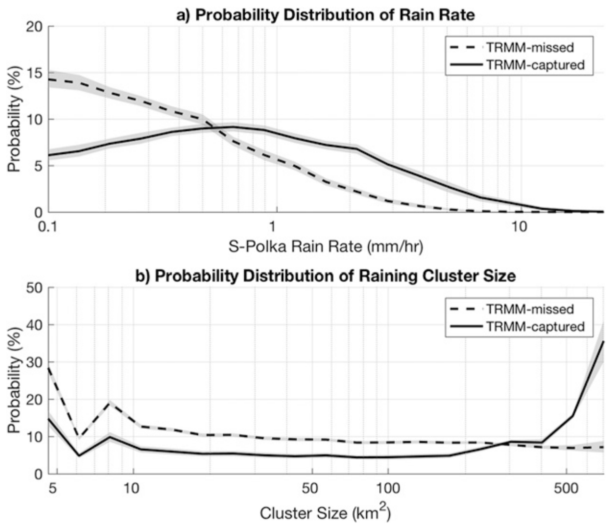

FIG. A2. (a) Probability of 3-hourly, 0.25° S-Polka rain rates within points where S-Polka identified some rain but TRMM classified as nonraining (dashed) and where both S-Polka and TRMM identified as raining (solid). (b) Frequency of occurrence by raining cluster size from S-Polka within the same set of grid points in (a). Raining cluster sizes are calculated after regridding the near-surface rain rates to 1 km × 1 km grids.

3B42 more frequently misses rain with small horizontal scales, which would appear more frequently during the MJO suppressed phase (Chen et al. 1996).

During the MJO enhanced phase, the diurnal peak of rain occurs around 0300–0600 LST in both TRMM 3B42 and S-Polka (Figs. A1e,f), consistent with Sakaeda et al. (2017). The distribution of the diurnal peak hours using the entire period is closer to the distribution during the MJO enhanced phase because there are more rain days during those periods. The major contrast between TRMM 3B42 and S-Polka appears in the distribution of the diurnal peak hour within the MJO suppressed phase (Figs. 1e,f). TRMM 3B42 has bimodal peaks around 0300–0600 and 1800 LST, while S-Polka has a primary peak at 0300 LST and a weaker, broader secondary peak at around 2100 LST.

The peak around 1800 LST in TRMM 3B42 during the MJO suppressed phase (Fig. A1e) was not apparent in some prior work using that dataset (Tian et al. 2006; Suzuki 2009; Oh et al. 2012; Sakaeda et al. 2017). The strong peak around 1800 LST partially results from differences in the sampling region. The peak at 1800 LST in TRMM becomes weaker and the peak at 0300–0600 LST becomes the stronger primary peak as we widen the sampling region within the Indian Ocean (not shown). Other likely reasons for the absence of the 1800 LST peak in Sakaeda et al. (2017) are the difference in sample time period and decadal drift in the frequency of microwave versus infrared (IR) rain estimates in TRMM 3B42 (Fig. A3). TRMM 3B42 combines rain-rate estimates by filling missing microwave data points with IR data (Huffman et al. 2007). Most of the microwave data come from sun-synchronized, polar-orbiting satellites, which cross the equator around the same local time, generating spurious diurnal variability due to aliasing. During the DYNAMO period over the S-Polka region, TRMM 3B42 rain rates are estimated by microwave data more frequently around 0200–0800 and 1400–2000 LST (Fig. A3a), while IR estimates are more frequently used during the intervening hours. Further complications arise because the equator crossing time changes because of orbital precession and the input number of satellite data changes over time (Huffman et al. 2007). Prior to 2005, the local times of most frequent microwave estimates were around 0900 and 2100 LST (Fig. A3b). Therefore, during those years, rain during the time of the secondary diurnal peak within the MJO suppressed phase (i.e., 1800 LST; Figs. A1e,f) was less frequently captured by microwave data. This likely contributes to the absence of the secondary afternoon peak in the diurnal phase within the MJO suppressed phase in studies that used earlier years of the TRMM 3B42 data (Oh et al. 2012; Rauniyar and Walsh 2011; Sakaeda et al. 2017).

The diurnal variability in the source of rain estimates in TRMM 3B42 contributes to the difference in the distribution of diurnal peak hour during the MJO suppressed phase between the TRMM and S-Polka (Figs. A1e,f). Gridpoint-by-gridpoint comparisons show that the TRMM 3B42 rain rate can drop sharply to zero as their source switches from microwave to IR, even while S-Polka continued to detect some rain (not shown). This underestimation by IR occurs more frequently during the MJO suppressed phase when total rain is predominantly composed of shallow warm clouds (not shown). Therefore, the diurnal variability in the frequency of microwave estimates in TRMM 3B42 can lead to artificial diurnal peak hours that are synchronized to microwave data availability, especially during the MJO suppressed phase. Henderson et al. (2017) also showed that biases in TRMM rain estimates from precipitation radar (PR) and radiometer (TMI) are dependent on precipitation regimes.

In conclusion, TRMM and S-Polka agree in the characteristics of the diurnal cycle of rain and how it changes between the enhanced and suppressed MJO phases. However, some discrepancy appears within the MJO suppressed phase because of prevalent light and small-scale rain that is not reliably measured by TRMM 3B42. A more detailed assessment of precise causes of the discrepancies between TRMM 3B42 and S-Polka is

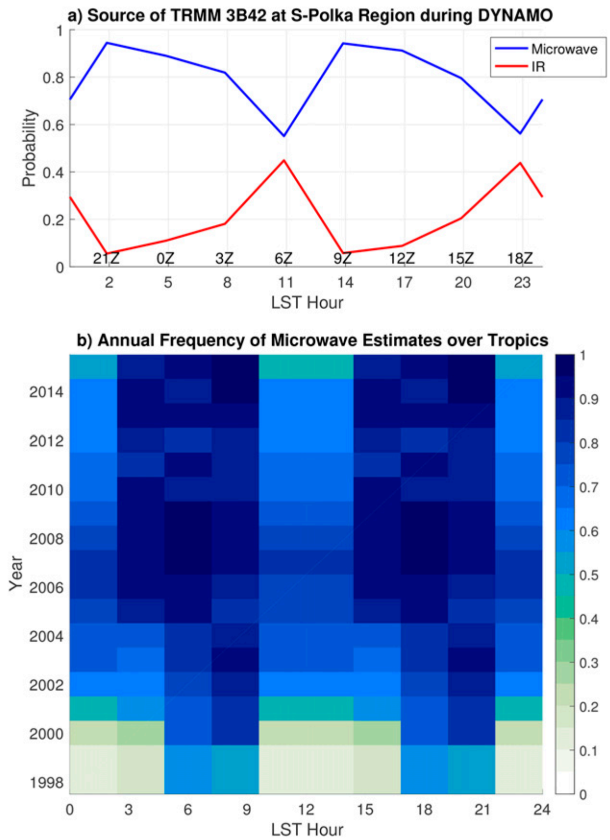

FIG. A3. (a) Frequency of TRMM 3B42 data sources from microwave and infrared over the S-Polka region during DYNAMO. (b) Annual frequency of TRMM 3B42 microwave estimates over all longitudes between 15°N and 15°S.

beyond the scope of this study. The quality of TRMM 3B42 and its comparison with the radar data are dependent on the regimes of large-scale variability (i.e., MJO enhanced versus suppressed). Future studies of the diurnal cycle of rainfall using TRMM 3B42 should take into account the higher uncertainties in the diurnal cycle during suppressed rainfall periods.

REFERENCES

Albright, M. D., E. E. Recker, R. J. Reed, and R. Dang, 1985: The diurnal variation of deep convection and inferred precipitation in the central tropical Pacific during January–February 1979. *Mon. Wea. Rev.*, **113**, 1663–1680, https://doi.org/10.1175/1520-0493(1985)113<1663:TDVODC>2.0.CO;2.

Barnes, H. C., and R. A. Houze Jr., 2013: The precipitating cloud population of the Madden-Julian Oscillation over the Indian and west Pacific Oceans. *J. Geophys. Res. Atmos.*, **118**, 6996–7023, https://doi.org/10.1002/jgrd.50375.

Benedict, J. J., and D. A. Randall, 2007: Observed characteristics of the MJO relative to maximum rainfall. *J. Atmos. Sci.*, **64**, 2332–2354, https://doi.org/10.1175/JAS3968.1.

Biasutti, M., S. E. Yuter, C. D. Burleyson, and A. H. Sobel, 2012: Very high resolution rainfall patterns measured by TRMM precipitation radar: seasonal and diurnal cycles. *Climate Dyn.*, **39**, 239–258, https://doi.org/10.1007/s00382-011-1146-6.

Cairns, B., 1995: Minimax workshop diurnal variations of cloud from ISCCP data. *Atmos. Res.*, **37**, 133–146, https://doi.org/10.1016/0169-8095(94)00074-N.

Chen, S. S., and R. A. Houze Jr., 1997: Diurnal variation and lifecycle of deep convective systems over the tropical Pacific warm pool. *Quart. J. Roy. Meteor. Soc.*, **123**, 357–388, https://doi.org/10.1002/qj.49712353806.

——, ——, and B. E. Mapes, 1996: Multiscale variability of deep convection in relation to large-scale circulation in TOGA COARE. *J. Atmos. Sci.*, **53**, 1380–1409, https://doi.org/10.1175/1520-0469(1996)053<1380:MVODCI>2.0.CO;2.

Ciesielski, P. E., and Coauthors, 2014: Quality-controlled upper-air sounding dataset for DYNAMO/CINDY/AMIE: Development and corrections. *J. Atmos. Oceanic Technol.*, **31**, 741–764, https://doi.org/10.1175/JTECH-D-13-00165.1.

DePasquale, A., C. Schumacher, and A. Rapp, 2014: Radar observations of MJO and Kelvin wave interactions during DYNAMO/CINDY2011/AMIE. *J. Geophys. Res. Atmos.*, **119**, 6347–6367, https://doi.org/10.1002/2013JD021031.

Dias, J., N. Sakaeda, G. N. Kiladis, and K. Kikuchi, 2017: Influences of the MJO on space-time tropical convection organization. *J. Geophys. Res. Atmos.*, **122**, 8012–8032, https://doi.org/10.1002/2017JD026526.

Frenkel, Y., B. Khouider, and A. J. Majda, 2011: Simple multicloud models for the diurnal cycle of tropical precipitation. Part I: Formulation and the case of the tropical oceans. *J. Atmos. Sci.*, **68**, 2169–2190, https://doi.org/10.1175/2011JAS3568.1.

Fujita, M., K. Yoneyama, S. Mori, T. Nasuno, and M. Satoh, 2011: Diurnal convection peaks over the eastern Indian ocean off Sumatra during different MJO phases. *J. Meteor. Soc. Japan*, **89A**, 317–330, https://doi.org/10.2151/jmsj.2011-A22.

Gray, W. M., and R. W. Jacobson, 1977: Diurnal variation of deep cumulus convection. *Mon. Wea. Rev.*, **105**, 1171–1188, https://doi.org/10.1175/1520-0493(1977)105<1171:DVODCC>2.0.CO;2.

Hannah, W. M., B. E. Mapes, and G. S. Elsaesser, 2016: A Lagrangian view of moisture dynamics during DYNAMO. *J. Atmos. Sci.*, **73**, 1967–1985, https://doi.org/10.1175/JAS-D-15-0243.1.

Henderson, D. S., C. D. Kummerow, D. A. Marks, and W. Berg, 2017: A regime-based evaluation of TRMM oceanic precipitation biases. *J. Atmos. Oceanic Technol.*, **34**, 2613–2635, https://doi.org/10.1175/JTECH-D-16-0244.1.

Huffman, G. J., and Coauthors, 2007: The TRMM Multisatellite Precipitation Analysis (TMPA): Quasi-global, multiyear, combined-sensor precipitation estimates at fine scales. *J. Hydrometeor.*, **8**, 38–55, https://doi.org/10.1175/JHM560.1.

Ichikawa, H., and T. Yasunari, 2006: Time–space characteristics of diurnal rainfall over Borneo and surrounding oceans as observed by TRMM-PR. *J. Climate*, **19**, 1238–1260, https://doi.org/10.1175/JCLI3714.1.

——, and ——, 2008: Intraseasonal variability in diurnal rainfall over New Guinea and the surrounding oceans during Austral summer. *J. Climate*, **21**, 2852–2868, https://doi.org/10.1175/2007JCLI1784.1.

Janowiak, J. E., P. A. Arkin, and M. Morrissey, 1994: An examination of the diurnal cycle in oceanic tropical rainfall using satellite and in situ data. *Mon. Wea. Rev.*, **122**, 2296–2311, https://doi.org/10.1175/1520-0493(1994)122<2296:AEOTDC>2.0.CO;2.

Johnson, R. H., and P. E. Ciesielski, 2013: Structure and properties of Madden–Julian oscillations deduced from DYNAMO sounding arrays. *J. Atmos. Sci.*, **70**, 3157–3179, https://doi.org/10.1175/JAS-D-13-065.1.

——, T. M. Rickenbach, S. A. Rutledge, P. E. Ciesielski, and W. H. Schubert, 1999: Trimodal characteristics of tropical convection. *J. Climate*, **12**, 2397–2418, https://doi.org/10.1175/1520-0442(1999)012<2397:TCOTC>2.0.CO;2.

——, P. E. Ciesielski, J. H. Ruppert Jr., and M. Katsumata, 2015: Sounding-based thermodynamic budgets for DYNAMO. *J. Atmos. Sci.*, **72**, 598–622, https://doi.org/10.1175/JAS-D-14-0202.1.

Kanamori, H., T. Yasunari, and K. Kuraji, 2013: Modulation of the diurnal cycle of rainfall associated with the MJO observed by a dense hourly rain gauge network at Sarawak, Borneo. *J. Climate*, **26**, 4858–4875, https://doi.org/10.1175/JCLI-D-12-00158.1.

Keeler, R. J., J. Lutz, and J. Vivekanandan, 2000: S-pol: NCAR's polarimetric Doppler research radar. *Proc. IGARS 2000: IEEE 2000 Int. Geoscience and Remote Sensing Symp.*, Honolulu, HI, IEEE, 1570–1573, https://doi.org/10.1109/IGARSS.2000.857275.

Kikuchi, K., and Y. N. Takayabu, 2004: The development of organized convection associated with the MJO during TOGA COARE IOP: Trimodal characteristics. *Geophys. Res. Lett.*, **31**, L10101, https://doi.org/10.1029/2004GL019601.

——, and B. Wang, 2008: Diurnal precipitation regimes in the global tropics. *J. Climate*, **21**, 2680–2696, https://doi.org/10.1175/2007JCLI2051.1.

Kiladis, G. N., K. H. Straub, and P. T. Haertel, 2005: Zonal and vertical structure of the Madden–Julian oscillation. *J. Atmos. Sci.*, **62**, 2790–2809, https://doi.org/10.1175/JAS3520.1.

Kim, J.-E., C. Zhang, G. N. Kiladis, and P. Bechtold, 2018: Heating and moistening of the MJO during DYNAMO in ECMWF reforecasts. *J. Atmos. Sci.*, https://doi.org/10.1175/JAS-D-17-0170.1, in press.

Kohyama, T., and J. M. Wallace, 2016: Rainfall variations induced by the lunar gravitational atmospheric tide and their implications for the relationship between tropical rainfall and humidity. *Geophys. Res. Lett.*, **43**, 918–923, https://doi.org/10.1002/2015GL067342.

Kraus, E. B., 1963: The diurnal precipitation change over the sea. *J. Atmos. Sci.*, **20**, 551–556, https://doi.org/10.1175/1520-0469(1963)020<0551:TDPCOT>2.0.CO;2.

Lau, K. H., and D. E. Waliser, 2011: *Intraseasonal Variability in the Atmosphere-Ocean Climate System.* Praxis, 646 pp.

Liebmann, B., and C. A. Smith, 1996: Description of a complete (interpolated) outgoing long-wave radiation dataset. *Bull. Amer. Meteor. Soc.*, **77**, 1275–1277.

Lindzen, R. S., 1978: Effect of daily variations of cumulonimbus activity on the atmospheric semidiurnal tide. *Mon. Wea. Rev.*, **106**, 526–533, https://doi.org/10.1175/1520-0493(1978)106<0526:EODVOC>2.0.CO;2.

Madden, R. A., and P. R. Julian, 1971: Detection of a 40–50-day oscillation in the zonal wind in the tropical Pacific. *J. Atmos. Sci.*, **28**, 702–708, https://doi.org/10.1175/1520-0469(1971)028<0702:DOADOI>2.0.CO;2.

——, and ——, 1972: Description of global-scale circulation cells in the tropics with a 40–50 day period. *J. Atmos. Sci.*, **29**, 1109–1123, https://doi.org/10.1175/1520-0469(1972)029<1109:DOGSCC>2.0.CO;2.

Majda, A. J., and Q. Yang, 2016: A multiscale model for the intraseasonal impact of the diurnal cycle over the Maritime Continent on the Madden–Julian oscillation. *J. Atmos. Sci.*, **73**, 579–604, https://doi.org/10.1175/JAS-D-15-0158.1.

Matthews, A. J., D. B. Baranowski, K. J. Heywood, P. J. Flatau, and S. Schmidtko, 2014: The surface diurnal warm layer in the Indian Ocean during CINDY/DYNAMO. *J. Climate*, **27**, 9101–9122, https://doi.org/10.1175/JCLI-D-14-00222.1.

Nesbitt, S. W., and E. J. Zipser, 2003: The diurnal cycle of rainfall and convective intensity according to three years of TRMM measurements. *J. Climate*, **16**, 1456–1475, https://doi.org/10.1175/1520-0442-16.10.1456.

Oh, J.-H., K.-Y. Kim, and G.-H. Lim, 2012: Impact of MJO on the diurnal cycle of rainfall over the western Maritime Continent in the austral summer. *Climate Dyn.*, **38**, 1167–1180, https://doi.org/10.1007/s00382-011-1237-4.

Peatman, S. C., A. J. Matthews, and D. P. Stevens, 2014: Propagation of the Madden–Julian oscillation through the Maritime Continent and scale interaction with the diurnal cycle of precipitation. *Quart. J. Roy. Meteor. Soc.*, **140**, 814–825, https://doi.org/10.1002/qj.2161.

——, ——, and ——, 2015: Propagation of the Madden–Julian oscillation and scale interaction with the diurnal cycle in a high-resolution GCM. *Climate Dyn.*, **45**, 2901–2918, https://doi.org/10.1007/s00382-015-2513-5.

Powell, S. W., and R. A. Houze Jr., 2013: The cloud population and onset of the Madden–Julian oscillation over the Indian Ocean during DYNAMO-AMIE. *J. Geophys. Res. Atmos.*, **118**, 11 979–11 995, https://doi.org/10.1002/2013JD020421.

——, and ——, 2015: Evolution of precipitation and convective echo top heights observed by TRMM radar over the Indian Ocean during DYNAMO. *J. Geophys. Res. Atmos.*, **120**, 3906–3919, https://doi.org/10.1002/2014JD022934.

——, ——, and S. R. Brodzik, 2016: Rainfall-type categorization of radar echoes using polar coordinate reflectivity data. *J. Atmos. Oceanic Technol.*, **33**, 523–538, https://doi.org/10.1175/JTECH-D-15-0135.1.

Randall, D. A., Harshvardhan, and D. A. Dazlich, 1991: Diurnal variability of the hydrologic cycle in a general circulation model. *J. Atmos. Sci.*, **48**, 40–62, https://doi.org/10.1175/1520-0469(1991)048<0040:DVOTHC>2.0.CO;2.

Rauniyar, S. P., and K. J. E. Walsh, 2011: Scale interaction of the diurnal cycle of rainfall over the Maritime Continent and Australia: Influence of the MJO. *J. Climate*, **24**, 325–348, https://doi.org/10.1175/2010JCLI3673.1.

Riley, E. M., B. E. Mapes, and S. N. Tulich, 2011: Clouds associated with the Madden–Julian oscillation: A new perspective from CloudSat. *J. Atmos. Sci.*, **68**, 3032–3051, https://doi.org/10.1175/JAS-D-11-030.1.

Ruppert, J. H., 2016: Diurnal timescale feedbacks in the tropical cumulus regime. *J. Adv. Model. Earth Syst.*, **8**, 1483–1500, https://doi.org/10.1002/2016MS000713.

——, and R. H. Johnson, 2015: Diurnally modulated cumulus moistening in the preonset stage of the Madden–Julian oscillation during DYNAMO. *J. Atmos. Sci.*, **72**, 1622–1647, https://doi.org/10.1175/JAS-D-14-0218.1.

——, and ——, 2016: On the cumulus diurnal cycle over the tropical warm pool. *J. Adv. Model. Earth Syst.*, **8**, 669–690, https://doi.org/10.1002/2015MS000610.

Sakaeda, N., G. Kiladis, and J. Dias, 2017: The diurnal cycle of tropical cloudiness and rainfall associated with the Madden–Julian oscillation. *J. Atmos. Sci.*, **30**, 3999–4020, https://doi.org/10.1175/JCLI-D-16-0788.1.

Schumacher, C., R. A. Houze Jr., and I. Kraucunas, 2004: The tropical dynamical response to latent heating estimates derived from the TRMM precipitation radar. *J. Atmos. Sci.*, **61**, 1341–1358, https://doi.org/10.1175/1520-0469(2004)061<1341:TTDRTL>2.0.CO;2.

Slingo, J., P. Inness, R. Neale, S. Woolnough, and G. Yang, 2003: Scale interactions on diurnal to seasonal timescales and their relevance to model systematic errors. *Ann. Geophys.*, **46**, 139–155, https://doi.org/10.4401/ag-3383.

Sui, C.-H., and K.-M. Lau, 1992: Multiscale phenomena in the tropical atmosphere over the western Pacific. *Mon. Wea. Rev.*, **120**, 407–430, https://doi.org/10.1175/1520-0493(1992)120<0407:MPITTA>2.0.CO;2.

——, ——, Y. N. Takayabu, and D. A. Short, 1997: Diurnal variations in tropical oceanic cumulus convection during TOGA COARE. *J. Atmos. Sci.*, **54**, 639–655, https://doi.org/10.1175/1520-0469(1997)054<0639:DVITOC>2.0.CO;2.

Suzuki, T., 2009: Diurnal cycle of deep convection in super clusters embedded in the Madden-Julian oscillation. *J. Geophys. Res.*, **114**, D22102, https://doi.org/10.1029/2008JD011303.

Tabata, Y., H. Hashiguchia, M. K. Yamamoto, M. Yamamoto, M. D. Yamanaka, S. Mori, F. Syamsudinc, and T. Manik, 2011: Observational study on diurnal precipitation cycle in equatorial Indonesia using 1.3-GHz wind profiling radar network and TRMM precipitation radar. *J. Atmos. Sol. Terr. Phys.*, **73**, 1031–1042, https://doi.org/10.1016/j.jastp.2010.10.003.

Thompson, E. J., S. A. Rutledge, B. Dolan, and M. Thurai, 2015: Drop size distributions and radar observations of convective and stratiform rain over the equatorial Indian and west Pacific Oceans. *J. Atmos. Sci.*, **72**, 4091–4125, https://doi.org/10.1175/JAS-D-14-0206.1.

——, ——, ——, ——, and V. Chandrasekar, 2018: Dual-polarization radar rainfall estimation over tropical oceans. *J. Appl. Meteor. Climatol.*, **57**, 755–775, https://doi.org/10.1175/JAMC-D-17-0160.1.

Tian, B., D. E. Waliser, and E. J. Fetzer, 2006: Modulation of the diurnal cycle of tropical deep convective clouds by the MJO. *Geophys. Res. Lett.*, **33**, L20704, https://doi.org/10.1029/2006GL027752.

Ueyama, R., and C. Deser, 2008: A climatology of diurnal and semi-diurnal surface wind variations over the tropical Pacific Ocean based on the tropical atmosphere ocean moored buoy array. *J. Climate*, **21**, 593–607, https://doi.org/10.1175/JCLI1666.1.

Waite, M. L., and B. Khouider, 2010: The deepening of tropical convection by congestus preconditioning. *J. Atmos. Sci.*, **67**, 2601–2615, https://doi.org/10.1175/2010JAS3357.1.

Xu, W., and S. A. Rutledge, 2014: Convective characteristics of the Madden–Julian Oscillation over the central Indian ocean observed by shipborne radar during DYNAMO. *J. Atmos. Sci.*, **71**, 2859–2877, https://doi.org/10.1175/JAS-D-13-0372.1.

——, and ——, 2015: Morphology, intensity, and rainfall production of MJO convection: Observations from DYNAMO shipborne radar and TRMM. *J. Atmos. Sci.*, **72**, 623–640, https://doi.org/10.1175/JAS-D-14-0130.1.

——, ——, C. Schumacher, and M. Katsumata, 2015: Evolution, properties, and spatial variability of MJO convection near and off the equator during DYNAMO. *J. Atmos. Sci.*, **72**, 4126–4147, https://doi.org/10.1175/JAS-D-15-0032.1.

Yanai, M., S. Esbensen, and J.-H. Chu, 1973: Determination of bulk properties of tropical cloud clusters from large-scale heat and moisture budgets. *J. Atmos. Sci.*, **30**, 611–627, https://doi.org/10.1175/1520-0469(1973)030<0611:DOBPOT>2.0.CO;2.

Yang, G.-Y., and J. Slingo, 2001: The diurnal cycle in the tropics. *Mon. Wea. Rev.*, **129**, 784–801, https://doi.org/10.1175/1520-0493(2001)129<0784:TDCITT>2.0.CO;2.

Yang, S., and E. A. Smith, 2006: Mechanisms for diurnal variability of global tropical rainfall observed from TRMM. *J. Climate*, **19**, 5190–5226, https://doi.org/10.1175/JCLI3883.1.

Yoneyama, K., C. Zhang, and C. N. Long, 2013: Tracking pulses of the Madden–Julian oscillation. *Bull. Amer. Meteor. Soc.*, **94**, 1871–1891, https://doi.org/10.1175/BAMS-D-12-00157.1.

Zuluaga, M. D., and R. A. Houze Jr., 2013: Evolution of the population of precipitating convective systems over the equatorial Indian ocean in active phases of the Madden–Julian Oscillation. *J. Atmos. Sci.*, **70**, 2713–2725, https://doi.org/10.1175/JAS-D-12-0311.1.